

Evidence of a Curved Synchrotron Spectrum in the Supernova Remnant SN 1006

G. E. Allen and J. C. Houck

*MIT Kavli Institute for Astrophysics and Space Research, Cambridge, MA 02139;
gea@space.mit.edu; houck@space.mit.edu*

and

S. J. Sturmer

*Astroparticle Physics Laboratory, Code 661, NASA Goddard Space Flight Center,
Greenbelt, MD 20771; sturmer@swati.gsfc.nasa.gov*

ABSTRACT

A joint spectral analysis of some *Chandra* ACIS X-ray data and Molonglo Observatory Synthesis Telescope radio data was performed for 13 small regions along the bright northeastern rim of the supernova remnant SN 1006. These data were fitted with a synchrotron radiation model. The nonthermal electron spectrum used to compute the photon emission spectra is the traditional exponentially cut off power law, with one notable difference: The power-law index is not a constant. It is a linear function of the logarithm of the momentum. This functional form enables us to show, for the first time, that the synchrotron spectrum of SN 1006 seems to flatten with increasing energy. The effective power-law index of the electron spectrum is 2.2 at 1 GeV (i.e., radio synchrotron-emitting momenta) and 2.0 at about 10 TeV (i.e., X-ray synchrotron-emitting momenta). This amount of change in the index is qualitatively consistent with theoretical models of the amount of curvature in the proton spectrum of the remnant. The evidence of spectral curvature implies that cosmic rays are dynamically important instead of being “test” particles. The spectral analysis also provides a means of determining the critical frequency of the synchrotron spectrum associated with the highest-energy electrons. The critical frequency seems to vary along the northeastern rim, with a maximum value of $1.1_{-0.5}^{+1.0} \times 10^{17}$ Hz. This value implies that the electron diffusion coefficient can be no larger than a factor of ~ 4.5 –21 times the Bohm diffusion coefficient if the velocity of the forward shock is in the range

2300–5000 km s⁻¹. Since the coefficient is close to the Bohm limit, electrons are accelerated nearly as fast as possible in the regions where the critical frequency is about 10¹⁷ Hz.

Subject headings: acceleration of particles — cosmic rays — ISM: individual (SN 1006) — radiation mechanisms: nonthermal — supernova remnants — X-rays: general

1. Introduction

Several observational and theoretical clues support the suggestion that Galactic cosmic rays, up to an energy of 100 TeV (Lagage & Cesarsky 1983) or more (Jokipii 1987; Völk & Biermann 1988; Bell & Lucek 2001), are accelerated predominantly in the shocks of supernova remnants. If Galactic supernovae occur at an average rate of one event every 30 years, then an average supernova remnant must transfer about 10% (Drury et al. 1989) of the initial 10⁵¹ ergs of kinetic energy of the ejecta to cosmic rays. In this case, the cosmic-ray energy density may be large enough to affect the structure of the shock (i.e., cosmic rays may not be mere “test” particles).

Three consequences of a large cosmic-ray pressure are potentially observable. One consequence is that the ambient material is slowed before it crosses the subshock. This effect reduces the temperature of the shocked gas (Chevalier 1983; Ellison et al. 2000; Decourchelle et al. 2000). An upper limit on the temperature is provided by the well-known relation between the shock speed v_s and the postshock temperature of a gas whose ratio of specific heats $\gamma = \frac{5}{3}$:

$$kT_i \leq \frac{3}{16}m_i v_s^2, \quad (1)$$

where k is Boltzmann’s constant and m_i and T_i are the mass and immediate postshock temperature, respectively, of particle species i . Since kinetic energy is transferred to cosmic rays at the expense of the thermalization of the shocked gas, the equality is appropriate only in the limit that the cosmic-ray energy density is negligible. Hughes et al. (2000) analyzed the transverse motion of the X-ray-emitting material (mostly reverse-shocked oxygen and neon) in the supernova remnant 1E 0102.2–7219 and inferred a forward-shock velocity $v_s = 6200_{-1600}^{+1500}$ km s⁻¹. In this case, the temperature of the shocked protons must be lower than the right-hand side of equation (1) or else the fitted electron temperature will be too low to be explained by Coulomb heating (Hughes et al. 2000). However, the proton temperature is sensitive to the shock velocity ($T \propto v_s^2$), and a variety of speeds are reported for 1E 0102.2–7219. Flanagan et al. (2004) report that the *Chandra* High Energy Transmission

Grating Ne X line emission data are consistent with a model that includes radial Ne X velocities up to $1800 \pm 450 \text{ km s}^{-1}$. Finkelstein et al. (2006) analyzed several features in O III images. The mean transverse velocity of the features is $2000 \pm 200 \text{ km s}^{-1}$. Eriksen et al. (2001) report that the motion of some O III-emitting material is best described by a radial O III velocity of about 1800 km s^{-1} . Since these velocity results differ and since none of the measurements provides a direct measure of the velocity of the forward shock, the claim that a significant fraction of the internal energy in 1E 0102.2–7219 has been transferred to cosmic rays requires additional support.

A second consequence is that the total compression ratio is larger than 4 (Ellison & Reynolds 1991; Berezhko & Ellison 1999). Since cosmic rays slow the upstream material before it crosses the subshock, the velocity of the shocked material relative to the subshock is reduced. As a result, the contact discontinuity is closer to the subshock than it would be in the absence of a large cosmic-ray pressure. Warren et al. (2005) report that in Tycho’s supernova remnant the mean ratio of the radius of the contact discontinuity to the radius of the forward shock is 0.93 ± 0.02 . This separation corresponds to a total compression ratio $r = 5.1_{-1.0}^{+1.9}$. Similarly, Cassam-Chenai et al. (2008) report that for the southeastern rim of SN 1006 the ratio varies from a value of $0.91_{-0.02}^{+0.03}$ (i.e., $r = 4.0_{-0.5}^{+2.2}$) between the bright X-ray synchrotron-emitting filaments to a value of 1 (i.e., $r = \infty$) along the filaments. The mean value between the filaments is 0.96 ± 0.03 (i.e., $r = 9.0_{-3.6}^{+25}$). These authors explore ways in which the location of the contact discontinuity can approach the location of the forward shock, but they cannot explain why these two features curiously appear to be coincident with one another along the filaments. Ksenofontov et al. (2005), who also studied SN 1006, infer a mean compression ratio $r = 5.2$.

A third consequence of a large cosmic-ray pressure is that the shock transition region is broadened or “smeared out” (Ellison & Reynolds 1991; Berezhko & Ellison 1999). Only the subshock has a short transition length. In this case, low-energy cosmic rays, which have relatively small diffusion lengths, experience only a portion of the velocity gradient as they scatter back and forth across the subshock. Higher energy particles, which have relatively large diffusion lengths, experience a larger portion (or all) of the velocity jump. Since the rate of energy gain increases as the velocity difference increases, higher energy particles gain energy faster than lower energy particles. As a result, cosmic-ray spectra do not have power-law distributions. The spectra flatten with increasing energy (Bell 1987; Ellison & Reynolds 1991; Berezhko & Ellison 1999). Jones et al. (2003) and Vink et al. (2006) report evidence of curvature in the synchrotron spectra of Cas A and RCW 86, respectively. One possible explanation for such curvature is that the cosmic-ray electrons producing the synchrotron emission have curved spectra.

Here we describe the results of an analysis of some radio and X-ray synchrotron data, which suggest that the synchrotron spectrum of SN 1006 might be curved. The data, assumptions, and analysis techniques are described in § 2. The results of the analysis are discussed in § 3. Our conclusions are summarized in § 4.

2. Data and analysis

X-ray spectra of the filaments along the northeastern rim of SN 1006 were obtained by analyzing 68 ks of data from the 2000 July 10–11 *Chandra*¹ observation of the source. The results of previous analyses of the data from this observation were published by Long et al. (2003) and Bamba et al. (2003). During the observation, the telescope was pointed at a location near the middle of the northeastern rim ($\alpha = 15^{\text{h}}03^{\text{m}}51.56^{\text{s}}$, $\delta = -41^{\circ}51'18.8''$; J2000). The X-rays were detected using the Advanced CCD Imaging Spectrometer (ACIS), which includes a 2×2 (ACIS-I) and a 1×6 (ACIS-S) array of CCDs. Six of these 10 detectors (ACIS-I2, -I3, -S1, -S2, -S3, and -S4) were used for the observation. Each $1024 \text{ pixel} \times 1024 \text{ pixel}$ CCD has a field of view of $8.4' \times 8.4'$. The angular resolution of the *Chandra* mirrors and ACIS varies over the observed portion of SN 1006 from about $0.5''$ at the aim point to $20''$ for a region that is $17.5'$ off-axis. The on-axis effective area for the mirrors and ACIS-S3 has a maximum of about 720 cm^2 at 1.5 keV and is greater than 10% of this value for energies between about 0.3 and 7.3 keV. The fractional energy resolution (FWHM/E) between these energies ranges from about 0.4 to 0.03, respectively. The sensitive energy bands and energy resolutions of the other five CCDs used for SN 1006 are typically narrower and worse, respectively, than the energy band and resolution of ACIS-S3.

The ACIS data were filtered to remove the events that (1) have $\text{GRADE} = 1, 5, \text{ or } 7$, (2) have one or more of the STATUS bits set to 1 (except for events that have only one or more of the four cosmic-ray “afterglow” bits set), (3) occur on a bad pixel or column, (4) are part of a serial readout streak on ACIS-S4, or (5) occur in the time interval during which the mean background count rate was more than twice the nominal rate (i.e., frames 20515–21294). An image of the 66 ks of “good” data is displayed in Figure 1. The $13, 100 \text{ pixel} \times 100 \text{ pixel}$ ($49'' \times 49''$) boxes are the regions of the bright, northeastern filaments used for the X-ray spectral analysis. The PHA spectra, ARFs, and RMFs for each region were created using version 2.3 of the CIAO² tools `dmextract`, `mkarf`, and `mkrmf`, respectively.

¹For more information about the *Chandra X-ray Observatory* refer to the *Chandra* Proposers’ Observatory Guide, which is available at <http://asc.harvard.edu/proposer/POG/index.html>.

²For more information about the CIAO analysis tools, refer to <http://asc.harvard.edu/ciao>.

The X-ray analysis was performed using data in the energy band 2–7 keV. The higher energy data were excluded because they are dominated by background events. The lower energy data were excluded for three reasons. First, a small, but noticeable, amount of thermal emission is evident at the lower energies. Therefore, inclusion of the lower energy data requires a spectral model that includes a thermal emission component. The extra parameters required to fit the thermal emission make the spectral fits unnecessarily complicated. By ignoring the data below 2 keV, nearly all of the thermal emission is excluded (Bamba et al. 2003). As displayed in Figure 1 (and as originally reported by Koyama et al. 1995), the high-energy nonthermal emission is concentrated along the rim. The second reason is that the ACIS detectors are not well calibrated at energies below about 0.7 keV. The last reason is that the absorption column density can be frozen at some preferred value to simplify the fitting process. Our preferred value is $n_{\text{H}} = 6.0 \times 10^{20} \text{ cm}^{-2}$, which is consistent with the results of Schaefer (1996) and Allen et al. (2001).

The radio data used for the spectral analysis include the compilation of flux density measurements listed in Table 1. These measurements are based on analyses of the emission from the entire supernova remnant. In the cases where no flux density uncertainties are reported, the uncertainties are assumed to be 10% of the reported flux densities. The results of the spectral analysis are insensitive to the actual fraction used at least for fractions in the range 5%–20%. The values listed in Table 1 are plotted in Figure 2. The dashed line in this figure is the result obtained when only the radio data are fitted with a power-law model: $S(\nu) = 17.6_{-4.8}^{+6.3}[\nu/(1 \text{ GHz})]^{-\alpha}$ Jy, where $\alpha = 0.60_{-0.09}^{+0.08}$. Note that the uncertainties for the power-law index and normalization, which are quoted at the 90% confidence level, are not independent. This result is an update of and consistent with the result reported by Allen et al. (2001): $S(\nu) = 17.9 \pm 1.1[\nu/(1 \text{ GHz})]^{-\alpha}$ Jy, where $\alpha = 0.57 \pm 0.06$. The dotted line in Figure 2 is a power-law model with the parameters reported by Green (2006): $S(\nu) = 19[\nu/(1 \text{ GHz})]^{-0.6}$ Jy.

The radio spectrum for the entire remnant is used to construct radio spectra for each region because there is little evidence of radio spectral variability. For example, a comparison of the images of Stephenson et al. (1977) and Gardner & Milne (1965) suggests that the slopes of the 0.408–2.7 GHz radio spectra of the northeastern and southwestern rims are about the same. It is possible that the slope may vary along each rim, in which case the best-fit amounts of curvature for individual regions may be inaccurate, but the mean amount of curvature for the 13 regions is relatively insensitive to such variations. Two sets of radio data were used with each X-ray spectrum. Both sets are obtained by multiplying the remnant-integrated flux densities and uncertainties of Table 1 by scaling factors ζ . One set of factors (Tables 2 and 3) is obtained by dividing the 843 MHz flux densities for the 13 regions marked with black squares in Figure 3, from the Molonglo Observatory Synthesis

Telescope (MOST), by the 843 MHz flux density for the entire remnant. These regions are the same ones used to obtain the X-ray spectra (Fig. 1). The second set of factors (Tables 4 and 5) is obtained in the same way, except that the flux densities for the 13 red squares are used instead of the flux densities for the black squares. The red squares are the regions where the flux densities peak. That is, the flux density along a line from the center of the remnant through the center of a black square peaks at the location of the center of the corresponding red square. Although both sets of flux densities represent local averages because the half-power beamwidth associated with the 843 MHz MOST image ($44'' \times 66''$; see Fig. 3) is comparable to the size of the regions ($49'' \times 49''$), they are reasonable estimates of the minimum (*black*) and maximum (*red*) flux densities for the 13 regions. Therefore, using these two sets of radio spectra provides a means of obtaining upper (Table 2) and lower (Table 4) limits on the amount of curvature for each region.

Version 1.4.8 of the spectral fitting package ISIS³ (Houck & DeNicola 2000) was used to fit the data for each region with a model that includes a synchrotron radiation component for the X-ray and radio data and an interstellar absorption component for the X-ray data (the XSPEC model `wabs`, with the relative abundances of Anders & Grevesse 1989). Since the 2–7 keV emission is dominated by nonthermal emission, no thermal X-ray component is included.

The synchrotron spectra are based on a nonthermal electron spectrum of the form

$$\frac{dn}{dp} = A \left(\frac{p}{p_0} \right)^{-\Gamma + a \log\left(\frac{p}{p_0}\right)} \exp\left(\frac{p_0 - p}{p_m} \right), \quad (2)$$

where n is the electron number density, $p = \gamma m v$ (γ , m , and v are the Lorentz factor, rest mass, and velocity of a particle, respectively), A is the number density at $p = p_0$ (in units of $p_0^{-1} \text{ cm}^{-3}$), $p_0 = 1 \text{ GeV } c^{-1}$ (c is the speed of light), Γ is the differential spectral index at $p = p_0$, a is the spectral “curvature,” the logarithm is base 10, and p_m is the exponential cutoff (or “maximum”) momentum. This form is the same as the standard power law with an exponential cutoff, except for the term $a \log(p/p_0)$. Introduction of this term produces an effective spectral index, $\Gamma_{\text{eff}} = \Gamma - a \log(p/p_0)$, that is a linear function of the logarithm of the momentum. For example, at momenta p of $10^0 p_0$, $10^1 p_0$, $10^2 p_0$, and $10^3 p_0$, the effective differential spectral indices are Γ , $\Gamma - a$, $\Gamma - 2a$, and $\Gamma - 3a$, respectively. If $a > 0$, then the spectrum flattens with increasing momentum. If $a < 0$, then the spectrum steepens with increasing momentum. If $a = 0$, then the spectrum has no curvature and equation (2) reduces to the standard power law with an exponential cutoff. An exponential cutoff is

³For more information about ISIS, see <http://space.mit.edu/cxc/isis>.

used in equation (2) for simplicity. Note that Ellison et al. (2001), Uchiyama et al. (2003), Lazendic et al. (2004), and Zirakashvili & Aharonian (2007) use a more general form for the cutoff ($\exp[-(p/p_m)^s]$, where $s = \frac{1}{4}, \frac{1}{2}, 1, \text{ or } 2$) and that Protheroe (2004) performed a detailed study of the shape of the cutoff for particles experiencing diffusive shock acceleration.

The synchrotron spectrum is computed by evaluating the following integral expression to obtain the differential photon flux⁴ (in SI units):

$$\frac{dF}{d(h\nu)} = \frac{V_S}{4\pi d^2} \frac{\sqrt{3}e^3 B}{2\epsilon_0 m c h^2 \nu} \int dp \frac{dn}{dp} \int_0^\pi d\theta \sin^2 \theta \frac{\nu}{\nu_c} \int_{\nu/\nu_c}^\infty dx K_{5/3}(x), \quad (3)$$

where V_S is the volume of the synchrotron-emitting region, d is the distance of the source from Earth, e is the unit of electric charge, B is the total magnetic field strength (not B_\perp), ϵ_0 is the permittivity of free space, h is Planck’s constant, ν is the frequency of an emitted photon, θ is the pitch angle between the electron momentum and magnetic field vectors, $K_{5/3}$ is an irregular modified Bessel function of the second kind, and

$$\nu_c = \frac{3e}{4\pi m^3 c^4} (p^2 c^2 + m^2 c^4) B \sin \theta \quad (4)$$

is the critical frequency of the synchrotron spectrum produced by an electron with a momentum p . The frequency at which a synchrotron power spectrum peaks is $\nu_p = 0.286\nu_c$. Hereafter, only the critical frequency ν_c is used.

We refer to the critical frequency associated with electrons that have a momentum equal to p_m as the “cutoff critical frequency” or just the cutoff frequency to emphasize that it is associated with electrons at the cutoff momentum of the electron spectrum [$\nu_m \equiv \nu_c(p = p_m)$]. The distribution of pitch angles θ is expected to be nearly isotropic because the forward-shock speed (2300–5000 km s^{−1}; Laming et al. 1996; Dwarkadas & Chevalier 1998; Ghavamian et al. 2002) is much less than the speed of light. In this case, the mean value of $\sin \theta$ in equation (4) is about $\pi/4$,

$$\nu_m = 1.26 \times 10^{17} \left(\frac{p_m}{10 \text{ TeV } c^{-1}} \right)^2 \left(\frac{B}{100 \text{ } \mu\text{G}} \right) \text{ Hz}, \quad (5)$$

and

$$h\nu_m = 0.522 \left(\frac{p_m}{10 \text{ TeV } c^{-1}} \right)^2 \left(\frac{B}{100 \text{ } \mu\text{G}} \right) \text{ keV}. \quad (6)$$

During the spectral fitting process, the right-hand side of equation (3) is computed each time the spectral fitting program changes the parameters of the model. The complete

⁴For more information about this model, see Houck & Allen (2006).

set of spectral parameters includes the spectral index Γ , the curvature parameter a , the cutoff momentum p_m , the total magnetic field strength B , the normalization constant $N_S = AV_S/4\pi d^2$, and the absorption column density n_H . The spectral index is determined by the radio and X-ray data. The curvature is sensitive to the relative radio and X-ray fluxes. Since only two of the three parameters p_m , B , and N_S are independent, p_m was fixed and the cutoff frequency ($\nu_m \propto p_m^2 B$; eq. [5]) is reported here instead of the magnetic field strength. This frequency is sensitive to the shape of the X-ray spectrum. The same normalization is used for both the X-ray and radio data for a given region because the nonthermal X-ray and radio emission from the region is assumed to be produced by a common population of electrons. The normalization N_S is determined by the radio data. The absorption column density n_H was fixed at the value $6.0 \times 10^{20} \text{ cm}^{-2}$ (Schaefer 1996; Allen et al. 2001).

Four spectral fits were performed for each region. The first pair are identical to one another except that the curvature parameter is a free parameter for one (Table 2) and is fixed at a value of zero (i.e., no spectral curvature) for the other (Table 3). In both cases, the radio spectra are normalized to the flux densities in the regions that are cospatial with the X-ray regions (i.e., the regions marked with black squares in Fig. 3). Since the cospatial radio spectra represent lower limits on the radio fluxes, the amounts of curvature listed in Table 2 are upper limits. The second pair of fits (Tables 4 and 5) is identical to the first pair except that the radio spectra are normalized to the flux densities in the “peak” regions (i.e., the regions marked with red squares in Fig. 3) instead of the cospatial regions. Since the peak radio spectra represent upper limits on the radio fluxes, the amounts of curvature listed in Table 4 are lower limits. For each of the four sets of fits, the best-fit values of the spectral index vary little from region to region, because the same radio spectral shape was used for each region. The best-fit model for region 6, the region with the largest number of counts, is plotted in Figures 2 and 4.

3. Discussion

It is not immediately obvious whether the cospatial or peak radio fluxes yield results that are more accurate, because the X-ray and radio synchrotron morphologies are not the same. For example, along 49''-wide strips that pass through the 13 X-ray regions toward the center of the remnant, one finds that the X-ray emission peaks at the locations of the black boxes in Figure 3 and that the radio emission peaks at the locations of the red boxes. There are at least three possible explanations for this difference. One explanation is that the TeV electrons that produce the X-ray synchrotron emission suffer significant synchrotron losses as they diffuse downstream from the shock. These losses deplete the highest-energy end of

the electron spectrum, causing the X-ray synchrotron emission to decline in the downstream region. As a result, the X-ray peak is relatively narrow and confined to a region near the shock. Since synchrotron losses are negligible for the GeV electrons that produce the radio emission, the radio emission is not attenuated in the same manner. The radio peaks can be broader and farther from the shock than the X-ray peaks. Nevertheless, there is no reason, on these grounds, to use different radio and X-ray extraction regions, because the radio and X-ray synchrotron emission for a region is produced by the same population of electrons. The radio emission is produced by the GeV portion of the electron spectrum and the X-ray emission is produced by the TeV segment. Synchrotron losses do not introduce a spatial separation between the GeV and TeV electrons.

Another explanation for the different X-ray and radio morphologies does involve an apparent (not actual) spatial separation. The X-ray and radio instruments do not yield images that have the same spatial resolution. The size of the spatially dependent point-spread function of the *Chandra* X-ray telescope is much smaller than the size of the $49'' \times 49''$ boxes and, hence, is neglected. However, the size of the beamwidth for the MOST image ($44'' \times 66''$) is not negligible, because it is comparable to the size of the boxes. The implications of the difference in the qualities of the X-ray and radio images are illustrated in Figure 5. The black histogram in the top panel shows the radial X-ray profile for region 6. The red curve in this panel is obtained by using a Gaussian function to smooth the histogram to the beamwidth of the radio instrument. Note that the peak of the red curve is about $18''$ downstream from the peak of the histogram, which suggests that the radio extraction region should be shifted toward the radio peak by the same amount. Similarly small shifts are obtained for the other 12 regions and for a simple model of a uniformly emitting spherical shell (Fig. 5, *bottom*).

A third explanation is that the bright radio-emitting region has expanded in the 17 intervening years between the time when the MOST data were obtained and the time of the *Chandra* observation. Using the mean radio expansion result of $0.049\% \pm 0.014\% \text{ yr}^{-1}$ (Moffett et al. 1993) suggests that the radio peak has shifted about $7.6'' \pm 2.2''$. To compensate for this expansion, the radio extraction region should be shifted toward the radio peak by the same amount. Since this shift and the apparent shift described above are small compared with the size of the extraction region, the following discussion focuses primarily on the results obtained using the cospatial radio fluxes.

3.1. Curvature

While the values of χ^2 per degree of freedom (dof) are acceptable for each of the four sets of fits, a comparison of Tables 2 and 3 (and of Tables 4 and 5) reveals that the values

are uniformly lower when curvature is included as a free parameter. For example, Figure 6 shows the 1, 2, and 3 σ confidence contours for region 6 in the parameter space defined by the electron spectral index Γ and the spectral curvature a . If the cospatial radio flux density is used, the results for this region suggest that an uncurved spectrum (i.e., the dashed line at $a = 0$) can be excluded at about the 2.7 σ confidence level. Similar results, with varying degrees of statistical significance, are obtained for the other 12 regions. Table 2 lists the probability $P_{\Delta\chi^2}$ that the reduction in the value of χ^2 when curvature is included as a free parameter is due to chance. The majority of the probabilities are less than 1%. Some are much less. The probabilities obtained using the F-test (P_F) are within a factor of 2 of the values listed in Table 2, except for regions 1, 2, 3, 5, 6, and 7, where $P_F = 0.058, 0.0035, 9.9 \times 10^{-6}, 0.0013, 0.0030,$ and 0.048 , respectively. The relatively large discrepancies between $P_{\Delta\chi^2}$ and P_F for these regions arise because the F-test depends on the value of χ^2/dof in addition to the value of $\Delta\chi^2$. Note that the values of χ^2/dof are significantly less than 1 for regions 1, 2, and 3 and that regions 5, 6, and 7 have the largest values of χ^2/dof . Since the values of $P_{\Delta\chi^2}$ are typically larger (i.e., less significant) than the values of P_F , only the values of $P_{\Delta\chi^2}$ are listed in Table 2. Collectively, these probabilities show that the spectra are significantly better fitted by a curved synchrotron model than an uncurved one.

The strength of this evidence depends on the location used to obtain the radio flux density. The radio flux density for a region increases from the cospatial location to the peak location. Since the appropriate location to use lies between these two, the cospatial and peak flux densities represent the lower and upper limits, respectively, on the radio flux density for the region. The amount of curvature depends on the relative X-ray and radio synchrotron fluxes. Therefore, the relatively small cospatial flux density yields an upper limit on the amount of curvature and the peak flux density yields a lower limit. Although the curvature values in Table 4 are lower limits, even these results favor a curved synchrotron model. Yet, as noted above, the upper limit values in Table 2 are expected to be closer to the actual amount of curvature because the appropriate location to use for the radio flux density is much closer to the cospatial location than the peak location.

The evidence of curvature cannot be attributed to an instrumental effect. It must be associated with the synchrotron spectrum of the source. For example, the need for curvature could be eliminated if the effective area of the X-ray detector system were too low, but the area would have to be in error by an implausibly large factor of about 4.6. The use of a curved source model is also compelling in the sense that the values of the best-fit indices and curvature parameters are consistent with the expected values. One expectation is that the best-fit index should be consistent with the radio spectral index. That is, the best-fit model should fit the radio spectrum instead of simply intersecting it. The mean value of the index $\Gamma = 2.221 \pm 0.013$ if curvature is included as a free parameter (Table 2). This

value is consistent with the index obtained if only the radio data are fitted with a power-law model ($\Gamma = 2\alpha + 1 = 2.20_{-0.18}^{+0.16}$; Fig. 2). Yet this result is not surprising, because the fitted value of the index is determined largely by the shape of the radio spectrum. For comparison, the mean value of the index $\Gamma = 2.031 \pm 0.017$ if an uncurved model is used (Table 3). This value differs significantly from 2.22 because the uncurved index, unlike the curved index, is sensitive to the relative radio and X-ray fluxes. While this result seems to be closer to the case of having the model simply intersect the radio spectrum, an index of 2.03 is still marginally consistent with the radio data because the radio data have relatively large uncertainties. Otherwise, the radio data might provide a means of discriminating between a curved and an uncurved model.

Another expectation is that the value of the curvature parameter should be positive. That is, the spectrum should flatten with increasing energy (Bell 1987; Ellison & Reynolds 1991; Berezhko & Ellison 1999). The results in Table 2 show that the best-fit values are greater than zero for all 13 regions. If the spectra are not curved, then the use of a curvature parameter may not be physically meaningful and one might expect roughly half of the values to be negative. If either sign is equally likely, then the chance probability that all 13 values have the same sign is 0.00024 (2^{-12}).

A third expectation is that the highest-energy electrons, the ones that experience the full strength of the shock and that produce the X-ray synchrotron emission, should have an effective spectral index of 2 (Berezhko et al. 2002). If equation (2) is an accurate representation of the shape of the electron spectrum, then the effective spectral index in the X-ray band $\Gamma_X = \Gamma - a \log(p_X/p_0)$, where p_X is the flux-weighted mean momentum of the electrons that produce the X-ray synchrotron radiation. To compute p_X from the fitted value of ν_m requires knowledge of the magnetic field strength (eq. [5]). Since the results of our analysis do not yield an estimate of the field strength, we assume that $p_X = 10 \text{ TeV } c^{-1}$. (The results are rather insensitive to this assumption as long as p_X is within an order of magnitude of $10 \text{ TeV } c^{-1}$.) In this case, $\Gamma_X = 2.005 \pm 0.027$. This index and the index obtained using the uncurved model ($\Gamma = 2.031_{-0.016}^{+0.017}$) are both consistent with the idea that the highest-energy electrons in SN 1006 have a spectral index of 2.0.

If the effective spectral index of the X-ray synchrotron-producing electrons $\Gamma_X = 2$ (aside from the exponential cutoff), then the expression for the effective spectral index can be inverted to obtain an estimate of the expected amount of curvature as a linear function of the spectral index Γ_r :

$$a_{\text{exp}} = \frac{\Gamma_r - 2}{\log(p_X/p_r)} \quad (7)$$

where Γ_r is the effective spectral index in the radio band and p_r is the flux-weighted mean momentum of the electrons that produce the radio synchrotron emission. Although the

value of p_X/p_r is unknown, $p_X/p_r = (\nu_X/\nu_r)^{1/2}$, where ν_X and ν_r are the critical frequencies associated with p_X and p_r , respectively. Since the X-ray data used here span the range from 2 to 7 keV, $\nu_X \approx 9.0 \times 10^{17}$ Hz, the logarithmic mid-point of this band. Similarly, $\nu_r \approx 660$ MHz, the logarithmic mid-point of the range from 86 MHz to 5 GHz (Table 1). These estimates yield $\log(p_X/p_r) = 4.57$. This value is rather insensitive to the uncertainties in ν_X and ν_r . For example, a change of a factor of 2 in the ratio ν_X/ν_r corresponds to a change of only 3.3% in $\log(p_X/p_r)$. As shown in Figure 6 (*dotted line*), a relation of the form $a_{\text{exp}} = (\Gamma_r - 2)/4.57$ is consistent with the confidence contours for region 6. This result is remarkable because the contours in Figure 6 are sensitive to the relative X-ray and radio fluxes, while equation (7) has no such dependence. Had the relative normalizations been significantly different, it is unlikely that the contours in Figure 6 would have been consistent with the dotted line. If Γ_r is accurately represented by the best-fit index (i.e., if $p_r \approx 1$ GeV c^{-1}) and if the cospatial radio fluxes are used, then $a_{\text{exp}} = (2.221 - 2)/4.57 = 0.048$. This expected value is consistent with the fitted value (0.054 ± 0.006) at the 90% confidence level. If the peak radio fluxes are used, then $a_{\text{exp}} = (2.198 - 2)/4.57 = 0.043$, which is less consistent with the fitted value ($0.033^{+0.007}_{-0.008}$). Like the expected radio flux, the expected amount of curvature lies between the cospatial and peak values. If the uncertainty associated with the radio flux leads to an uncertainty in the amount of curvature comparable to the statistical uncertainty, then the amount of curvature is most likely 0.05 ± 0.01 .

Not only is the best-fit amount of curvature consistent with equation (7), it is also consistent with the amount of curvature predicted for the proton (not electron) spectrum of SN 1006. For example, Figure 7 shows the best-fit electron spectra for region 6. The spectra are not curved below $p = 1$ GeV c^{-1} , which was true during the fitting process, because the available data poorly constrain the shape of the electron spectrum in this momentum range. The top pair of dotted and dot-dashed curves are predictions described by Ellison et al. (2000) for the proton (not electron) spectrum of SN 1006. These spectra have been normalized to match the solid black curve at $E = 0.9$ GeV. Since Ellison et al. (2000) computed their spectrum assuming a spectral index $\Gamma = 2.0$, it is not appropriate to compare the solid curve with the upper pair of dotted and dot-dashed curves. However, the lower pair of dotted and dot-dashed curves have been multiplied by the energy-dependent factor $[E/(0.9 \text{ GeV})]^{-0.2}$ to match the best-fit spectral index $\Gamma = 2.2$. Aside from a possible difference in the assumed value of the cutoff momentum, the lower pair of theoretical curves match the solid black curve remarkably well.

The evidence of curvature is based on a set of assumptions. One assumption is that the electron spectrum has the form of equation (2). This functional form excludes the effects of a synchrotron cooling break (Völk et al. 2005). If the magnetic field strength is as large as 150 μG , then synchrotron cooling may significantly steepen the highest-energy end of

the electron spectrum (Ksenofontov et al. 2005). Since the fits are sensitive only to the net amount of curvature between radio and X-ray frequencies, inclusion of a cooling break would require a larger amount of curvature (i.e., more flattening than the amount of curvature reported here) to compensate for the spectral steepening of the cooling break. Another assumption is that the shape of the radio spectrum in each of the 13 regions is the same as the shape of the radio spectrum of the entire remnant. If this assumption is invalid, then the best-fit values of the spectral index and curvature may be inaccurate for any given region. Yet, the mean values of the index and curvature are insensitive to such spatial variations. A third assumption is that the shape of the synchrotron spectrum is uniform inside each of the 13 regions. Some young remnants, such as Cas A (Anderson & Rudnick 1996) and Kepler (DeLaney et al. 2002), exhibit evidence of radio spectral variations from one region to another. Therefore, the combination of the synchrotron spectra of several small-scale features might naturally yield a curved composite spectrum even if the synchrotron spectrum for each feature is just a power law. Small extraction regions were used to minimize this problem. A fourth assumption is that our estimates of the fraction of the 843 MHz flux from each region are accurate. As discussed above, the size of the beamwidth leads to some uncertainty about the proper radio fluxes to use for each region. Yet, even the worst-case scenario, the results obtained using the peak radio fluxes, requires some spectral curvature. High-quality radio and X-ray spectra for many, small, spatially resolved features in the remnant would eliminate the need for many of these assumptions. Unfortunately, these kinds of data are not available for SN 1006.

Evidence of curvature in the synchrotron spectra of supernova remnants has been reported previously. Reynolds & Ellison (1992) analyzed the remnant-integrated radio spectra of Kepler, Tycho, and SN 1006. They find hints of curvature for Tycho and Kepler. Unfortunately, a careful study of the radio emission from Kepler (DeLaney et al. 2002) reveals intrinsic variations in the radio spectral index from region to region. Therefore, it is not possible to dismiss the idea that the evidence of curvature in the remnant-integrated spectrum is the result of the combination of several power-law spectra with different spectral indices. Jones et al. (2003) minimized this problem for Cas A by analyzing the radio-to-infrared synchrotron spectra of small, selected features in the remnant. The results of their analysis indicate that the spectra of these regions flatten with increasing energy. We find that their spectra can be fitted with our curved spectral model if the curvature parameter $a = 0.06 \pm 0.01$. It is interesting that this value is consistent with the mean amount of curvature for SN 1006 (0.05 ± 0.01). Based on an analysis of X-ray data for a small feature on the northeastern shell of RCW 86, Vink et al. (2006) report evidence of curvature in the synchrotron spectrum of this remnant. This claim would be strengthened if the data were fitted with a model that includes the spectral index as a free parameter and if there were

similar evidence for more than one feature in the remnant.

The evidence of curvature suggests that the pressure exerted by nonthermal particles is large enough to modify the structure of the shock. The cosmic-ray pressure is most likely dominated by nuclei, not electrons. For example, analyses of the synchrotron spectrum of SN 1006 have been used to estimate the total energy of the nonthermal electrons in the remnant. These estimates, which depend on the assumed value of the mean magnetic field strength, include 5×10^{47} ergs (for $B = 150 \mu\text{G}$; Berezhko et al. 2002), 9×10^{47} ergs (for $B = 40 \mu\text{G}$; Allen et al. 2001), and 7×10^{48} ergs (for $B = 3 \mu\text{G}$; Dyer et al. 2001). The remnant was recently observed with the H.E.S.S. gamma-ray telescope (Aharonian et al. 2005). If the upper limits on the TeV gamma-ray flux reported by Aharonian et al. (2005) are accurate (cf. Tanimori et al. 1998), then a combination of these constraints and the measured synchrotron flux can be used to show that the mean magnetic field strength must be at least $25 \mu\text{G}$ (Aharonian et al. 2005). In this case, the total energy in cosmic-ray electrons is probably no larger than about 10^{48} ergs. Since this energy is a small fraction of the total internal energy ($\sim 10^{51}$ ergs), the nonthermal electron pressure is most likely a small fraction of the ram pressure at the shock. Yet, the total energy in cosmic-ray nuclei, which may be about 2 orders of magnitude larger than the total energy in cosmic-ray electrons, could be large enough to modify the structure of the shock.

3.2. Cutoff Frequency and Diffusion Coefficient

In addition to providing evidence of curvature, fits to the synchrotron spectral data provide a measure of the frequency at which the synchrotron spectrum is cut off (eq. [5]). The results for the cutoff critical frequency are listed in Tables 2–5. A comparison of Tables 2 and 3 (and of Tables 4 and 5) reveals that the frequencies for the curved spectra are somewhat lower than the frequencies for the uncurved spectra because positive curvature causes a synchrotron spectrum to flatten with increasing energy. To compensate, the X-ray synchrotron spectrum is steepened by reducing the cutoff frequency. The solid and dashed black lines in Figure 7 show that the two effects more or less offset one another to produce electron (and, hence, synchrotron) spectra that have nearly the same shape in the X-ray synchrotron-emitting band.

Bamba et al. (2003), Rothenflug et al. (2004), and Bamba et al. (2008) fitted X-ray spectra for the bright rims of SN 1006 with models that include the XSPEC synchrotron component `srcut`. Since `srcut` does not include spectral curvature, their results should be compared with the results listed in Table 3. To the extent that the regions used by Bamba et al. (2003) and Rothenflug et al. (2004) are similar to the regions used here, this

comparison reveals that their cutoff frequencies are systematically higher than the frequencies listed in Table 3. This difference is due, in part, to a difference in the spectral indices. Our best-fit spectral indices ($\Gamma = 1.98\text{--}2.12$; Table 3) are lower than the indices used by Bamba et al. (2003; $\Gamma = 2.14$) and Rothenflug et al. (2004; $\Gamma = 2.2$). While an index of about 2.2 is appropriate for the radio synchrotron-emitting electrons (i.e., the electrons at momenta $p \sim 1 \text{ GeV } c^{-1}$), an index of 2.0 seems to better describe the X-ray synchrotron-emitting electrons (i.e., the electrons at momenta $p \sim 10 \text{ TeV } c^{-1}$). For example, if the electron spectrum is not curved, then the mean index is 2.031 ± 0.017 (Table 3). If curvature is included, then the effective mean index at 10 TeV is 2.005 ± 0.027 [i.e., $2.221 \pm 0.013 - (0.054 \pm 0.006) \log(10 \text{ TeV}/1 \text{ GeV})$; Table 2]. In both cases, the results imply that the index near the cutoff of the electron spectrum is about 2.0, which is consistent with the model of Berezhko et al. (2002). Berezhko et al. note that the electron spectrum is steeper at radio synchrotron-emitting momenta than at X-ray synchrotron-emitting momenta because GeV electrons sample only a portion of the shock while the highest-energy electrons “see” the full strength of the shock. Although the same argument applies to the results of Bamba et al. (2008), who use a spectral index $\Gamma = 2.14$, their best-fit break frequency for the entire northeastern rim is lower than the mean value of ν_m in Table 3 [$\bar{\nu}_m = (9.07 \pm 0.98) \times 10^{16} \text{ Hz}$]. If the normalization of the synchrotron spectrum is too high, then the best-fit frequency may be reduced. While the normalization reported by Bamba et al. (2008; 7.72 Jy at 1 GHz) is approximately correct for the entire northeastern rim, only the flux density of the portion of the rim associated with the very narrow region in which the X-ray synchrotron emission is produced should be used. For these reasons, we believe that the cut-off frequencies reported here are relatively accurate.

The frequencies listed in Tables 2 and 3 are plotted in Figure 8 as a function of the position angles of the regions. This angle is measured relative to the location of the center of the remnant (Fig. 1) and is expressed in degrees from north (0°) through east (90°). As shown in Figure 8, there may be an azimuthal variation in the value of the cutoff frequency. A constant value [i.e., the weighted mean value of $(4.98 \pm 0.67) \times 10^{16} \text{ Hz}$, 90% confidence level uncertainties] can be excluded at the 2.5σ confidence level. Rothenflug et al. (2004) also report evidence of an azimuthal variation in the cutoff frequency. Since the frequency $\nu_m \propto p_m^2 B$, these results imply that the cutoff momentum of the electron spectrum and/or the magnetic field strength varies along the northeastern rim. Since it is not possible to independently determine both p_m and B using the synchrotron spectral data alone, the present analysis does not provide a means of identifying the cause of a variation in the cutoff frequency.

As described in the Appendix, it is possible to use a fitted value of the cutoff critical frequency to constrain the mean electron diffusion coefficient $\bar{\kappa}$. The upper limit on $\bar{\kappa}$, as a

fraction of the mean Bohm diffusion coefficient $\bar{\kappa}_B$, depends on the forward-shock velocity u_1 , the cutoff critical frequency ν_m , and a function f of the compression ratio r and the ratio of the upstream to downstream magnetic field strengths B_1/B_2 (eqs. [A5]–[A8]).⁵ If $u_1 = 2300\text{--}5000 \text{ km s}^{-1}$ (Laming et al. 1996; Dwarkadas & Chevalier 1998; Ghavamian et al. 2002), $\nu_m = 1.1 \times 10^{17} \text{ Hz}$ (Table 2), and $f = 0.1875$ (i.e., $r = 4$ and $B_1/B_2 \approx 0$), then $\bar{\kappa} \leq (4.5\text{--}21)\bar{\kappa}_B$. If the compression ratio is 5.2 (Ksenofontov et al. 2005) instead of 4, then $f = 0.155$ and $\bar{\kappa} \leq (3.7\text{--}18)\bar{\kappa}_B$. If the cutoff frequency is about 10^{18} Hz (Rothenflug et al. 2004) instead of 10^{17} Hz , then $\bar{\kappa} \leq (0.5\text{--}2.3)\bar{\kappa}_B$. In each of these cases, the highest-energy electrons have diffusion coefficients nearly as small as the Bohm coefficient (i.e., are being accelerated about as fast as possible).

Similar results for the diffusion coefficient are reported by Bamba et al. (2003), Yamazaki et al. (2004), and Parizot et al. (2006). The latter two of these three use equations similar to equation (A5) but obtain significantly smaller limits for the diffusion coefficient because they use much larger cutoff critical frequencies (9.1×10^{17} and $2.5 \times 10^{18} \text{ Hz}$, respectively, instead of $1.1 \times 10^{17} \text{ Hz}$). Bamba et al. (2003) take a different approach. They assume that the width ($\psi_1 d$) of the part of a filament that is in the upstream region is determined by the diffusion length (κ_1/u_1) in this region. In this case,

$$\frac{\kappa_1}{\kappa_{B,1}} = \left(\frac{27e^3}{4\pi m^3 c^4} \right)^{1/2} \left(\frac{B_1^3 \sin \theta_1}{\nu_{m,1}} \right)^{1/2} \psi_1 d u_1 \quad (8)$$

$$= 0.00262 \left(\frac{B_1}{3 \mu\text{G}} \right)^{3/2} \left(\frac{\psi_1}{1 \text{ arcsec}} \right) \left(\frac{d}{1 \text{ kpc}} \right) \left(\frac{u_1}{10^3 \text{ km s}^{-1}} \right) \left(\frac{\nu_{m,1}}{10^{17} \text{ Hz}} \right)^{-1/2}, \quad (9)$$

where κ_1 , $\kappa_{B,1}$ [= $pc/(3eB_1)$], B_1 , $\nu_{m,1}$, and ψ_1 are the diffusion coefficient, Bohm diffusion coefficient, mean magnetic field strength, cutoff critical frequency, and filament width,⁶ respectively, in the upstream region and u_1 is the velocity of the forward shock. The numerical constant in equation (9) was computed assuming that the value of $\sin \theta_1$ is $\pi/4$, the isotropic mean value. Like equation (A5), equation (9) is valid only at the momentum $p = p_m$. If the value of B_1 is comparable to a typical interstellar field strength (e.g., $3 \mu\text{G}$), then, for reasonable values of ψ_1 , d , u_1 , and $\nu_{m,1}$, κ_1 is uncomfortably small compared with the Bohm diffusion coefficient. There are at least three explanations for this apparent dilemma. One explanation is that, near the shock, B_1 may be amplified by cosmic-ray

⁵The corresponding upper limit on the diffusion length $l_m \approx \bar{\kappa}/u_1$ (Lagage & Cesarsky 1983). Using eqs. (4) and (A4) yields $l_m \propto f u_1 \nu_{m,2}^{-1/2} B_2^{-3/2}$. If $f = 0.1875$, $u_1 = 2300\text{--}5000 \text{ km s}^{-1}$, $\nu_{m,2} = 10^{17} \text{ Hz}$, and $B_2 > 25 \mu\text{G}$ (Aharonian et al. 2005), then $l_m < 0.17\text{--}0.36 \text{ pc}$ (i.e., $l_m/d < 16''\text{--}34''$ if $d = 2.2 \text{ kpc}$; Winkler et al. 2003).

⁶Here ψ_1 is the actual angular width, not the observed angular width.

streaming (Lucek & Bell 2000; Bell & Lucek 2001; Bell 2004). For example, equation (15) of Bell & Lucek (2001) yields $B_1 = 30 \mu\text{G}$ (see Ksenofontov et al. 2005) and, hence, $\kappa_1 \sim \kappa_{\text{B},1}$, if the upstream mass density $\rho_1 = 2.4 \times 10^{-25} \text{ g cm}^{-3}$ (i.e., $n_1 = 0.1 \text{ cm}^{-3}$), the shock velocity $u_1 = 2300\text{--}5000 \text{ km s}^{-1}$, and the cosmic-ray pressure is about 30%–14% of the ram pressure, respectively. Another explanation, which is mentioned by Yamazaki et al. (2004), is that the rate of acceleration can exceed the Bohm limit (i.e., κ_1 can be less than $\kappa_{\text{B},1}$) if the magnetic field is parallel to the shock (see Jokipii 1987). A third explanation is that the width of a filament represents the size of the region in which the magnetic field is strong (Pohl et al. 2005) instead of the diffusion length. In this case, equations (8) and (9) are not useful because an assumption upon which they are based is not valid.

Independent of the technique used to estimate or constrain the diffusion length, it seems likely that the highest-energy electrons in SN 1006 are diffusing close to the Bohm limit. Otherwise, the rate of acceleration is too low for electrons to reach energies high enough to produce the observed X-ray synchrotron radiation. Yet, it is important to note that the limit on the diffusion coefficient described in the Appendix (and the value obtained using eqs. [8] and [9]) is only an estimate, for the following reasons:

1. The fitted values of the cutoff frequency are sensitive to the assumed shape of the electron spectrum at momenta near the cutoff in the electron spectrum. The actual functional form of the electron spectrum may be significantly more complicated than equation (2). As an example of the extent to which differences in the shape of the electron spectrum can affect the limit, consider the results obtained using the models with and without curvature. If the curved model is used, then the maximum cut-off critical frequency is $1.1 \times 10^{17} \text{ Hz}$ (Table 2) and $\bar{\kappa} \leq (4.5\text{--}21)\bar{\kappa}_{\text{B}}$ (for $f = 0.1875$, $B_1/B_2 \approx 0$, and $u_1 = 2300\text{--}5000 \text{ km s}^{-1}$). If the model does not include curvature, then $\nu_m = 3.0 \times 10^{17} \text{ Hz}$ (Table 3) and $\bar{\kappa} \leq (1.7\text{--}7.8)\bar{\kappa}_{\text{B}}$.

2. There is evidence that the cutoff frequency varies from one region to another in SN 1006 (Fig. 8; Rothenflug et al. 2004). Here the frequency used to compute the limit is the largest value in Table 2. Therefore, our constraint on the diffusion coefficient of SN 1006 applies only to the region where the cutoff frequency is largest. The limits for other regions of the remnant are larger.

3. The limit is computed assuming that the electron momentum $p = p_m$. Therefore, the limit only applies to electrons at the cutoff momentum [i.e., $\bar{\kappa} = \bar{\kappa}(p = p_m)$]. An advantage to using this momentum is that the limit does not depend on the functional form of $\bar{\kappa}(p)$.

4. The limit is based on the assumption that the cutoff is due to synchrotron losses. If some other process, such as the escape of electrons from the acceleration region or the length of time over which particles are accelerated, determines the cutoff momentum, then

the diffusion coefficient is lower than the right-hand side of equation (A5). If this equation yields a limit close to 1, then the results indicate that synchrotron losses are important for electrons that have momenta $p \geq p_m$.

5. The value of the function f depends on the unknown compression ratio and the unknown ratio of the upstream to downstream magnetic field strengths (eq. [A7]). A value of $f = 0.1875$ (i.e., $r = 4$ and $B_1/B_2 \approx 0$) is used here because the compression ratio is probably at least as large as 4 (Blondin & Ellison 2001; Ksenofontov et al. 2005; Warren et al. 2005; Cassam-Chenai et al. 2008). If $r > 4$, then $f < 0.1875$ and our upper limit on the diffusion coefficient is overestimated. Likewise, the upper limit is overestimated if B_1/B_2 is significantly larger than zero.

6. Equation (A5) was derived assuming an isotropic pitch-angle distribution. While such a distribution is expected if electrons diffuse in the Bohm limit, the actual distribution may be different.

4. Conclusions

We have performed a joint spectral analysis of some *Chandra* ACIS X-ray data and MOST radio data for 13 small regions along the bright northeastern rim of the supernova remnant SN 1006. The data were fitted with a model that includes a synchrotron emission component. This component is based on an electron spectrum that has a momentum-dependent spectral index. The rate of change in the index for each decade in momentum is a free parameter of the fit. If the assumptions described in § 3.1 are valid, then the results of the spectral analysis, which show that the synchrotron spectra of SN 1006 are curved, can be interpreted as evidence of curvature in the GeV-to-TeV electron spectra. The mean amount of curvature in the electron spectra is qualitatively consistent with predictions of the amount of curvature in the proton spectrum of SN 1006 (Ellison et al. 2000). The best-fit power-law index at 1 GeV (i.e., at radio synchrotron-emitting momenta) is $2.221^{+0.013}_{-0.012}$. Including the effect of curvature, the effective spectral index at about 10 TeV (i.e., at X-ray synchrotron-emitting momenta) is 2.005 ± 0.027 (90% confidence level uncertainties). This effective index is consistent with the predictions of Berezhko et al. (2002).

The evidence of curved electron spectra suggests that cosmic rays are not “test” particles. The cosmic-ray pressure at the shock is large enough to modify the structure of the shock. Since nonthermal electrons contain only about 0.1% (i.e., 10^{48} ergs) or less of the total internal energy, the results provide indirect evidence of a much more energetic population of cosmic-ray protons. Collectively, the evidence of (1) spectral curvature in Cas A

(Jones et al. 2003), RCW 86 (Vink et al. 2006), and SN 1006, (2) an unusually low electron temperature in 1E 0102.2–7219 (Hughes et al. 2000), and (3) a compression ratio greater than 4 in Tycho (Warren et al. 2005) and SN 1006 (Cassam-Chenai et al. 2008) suggests that efficient particle acceleration may be a common feature of young, shell-type supernova remnants.

The results of the spectral analysis also determine the “cutoff critical frequency” ν_m . This frequency seems to vary from one region to another (see also Rothenflug et al. 2004), which implies that the exponential cutoff momentum of the electron spectrum and/or the strength of the magnetic field varies. It is not possible to identify the cause of the variation using the synchrotron spectral data alone.

As described in the Appendix, the cutoff frequency can be used to set an upper limit on the mean diffusion coefficient $\bar{\kappa}$ of the highest-energy electrons. Aside from the cutoff frequency, this limit depends (strongly) on the velocity of the forward shock u_1 and (weakly) on the compression ratio r and the ratio of the upstream to downstream magnetic field strengths B_1/B_2 . If $\nu_m = 1.1 \times 10^{17}$ Hz, $u_1 = 2300\text{--}5000$ km s $^{-1}$, $r = 4$, and $B_1/B_2 \approx 0$, then $\bar{\kappa} < (4.5\text{--}21)\bar{\kappa}_B$, where $\bar{\kappa}_B$ is the mean Bohm diffusion coefficient. This result implies that at least some of the highest-energy electrons in SN 1006 diffuse close to the Bohm limit (i.e., are accelerated about as fast as possible), which provides additional support for the idea that Galactic cosmic rays are predominantly accelerated by the shocks of supernova remnants.

We gratefully acknowledge the guidance of Don Ellison. This work grew out of discussions with him regarding the shape of cosmic-ray spectra. We thank Chuck Dermer, whose encouragement led us to develop a synchrotron model for a curved electron spectrum. This work benefited substantially from discussions with Tom Jones and Steve Reynolds and from comments by the anonymous referee. G. E. A. and J. C. H. are supported by contract SV3-73016 between MIT and the Smithsonian Astrophysical Observatory. The Chandra X-Ray Center at the Smithsonian Astrophysical Observatory is operated on behalf of NASA under contract NAS8-03060.

A. Diffusion coefficient

This appendix describes how measurements of or inferences about the shock velocity and cutoff frequency can be used to place an upper limit on the electron diffusion coefficient. Since the mean rate of synchrotron losses cannot exceed the mean rate of energy gains at

momenta below the cutoff of the electron spectrum,

$$\left(\frac{dE}{dt}\right)_{\text{acc}} \geq -\left(\frac{dE}{dt}\right)_{\text{sync}} \quad (\text{A1})$$

in this range. The rate of acceleration at $p = p_m \gg mc$ is given by

$$\left(\frac{dE}{dt}\right)_{\text{acc}} = \frac{p_m c}{3} \left(\frac{\kappa_1}{u_1} + \frac{\kappa_2}{u_2}\right)^{-1} (u_1 - u_2) \quad (\text{A2})$$

(Lagage & Cesarsky 1983). If the rates of synchrotron losses in the upstream and downstream regions are weighted by the mean residence times in these regions [$\Delta t_1 = 4\kappa_1/(u_1 v)$ and $\Delta t_2 = 4\kappa_2/(u_2 v)$; Webb et al. 1984], then

$$-\left(\frac{dE}{dt}\right)_{\text{sync}} = \frac{e^4}{6\pi\epsilon_0 m^4 c^3} p_m^2 \left(\frac{\kappa_1}{u_1} B_1^2 \sin^2 \theta_1 + \frac{\kappa_2}{u_2} B_2^2 \sin^2 \theta_2\right) \left(\frac{\kappa_1}{u_1} + \frac{\kappa_2}{u_2}\right)^{-1} \quad (\text{A3})$$

(Blumenthal & Gould 1970), where κ_1 and κ_2 are the upstream and downstream electron diffusion coefficients perpendicular to the shock, u_1 and u_2 are the speeds of the upstream and downstream material relative to the shock, v is the velocity of a particle, ϵ_0 is the permittivity of free space, B_1 and B_2 are the mean upstream and downstream magnetic field strengths, and θ_1 and θ_2 are the pitch angles between the electron momentum and magnetic field vectors in the upstream and downstream regions, respectively. If $\sin \theta$ in equation (4) is replaced by the isotropic mean value of $\pi/4$ and if $\sin^2 \theta_1$ and $\sin^2 \theta_2$ in equation (A3) are replaced by the isotropic mean value of $\frac{2}{3}$, then a combination of equations (4), (A1), (A2), and (A3) yields

$$\frac{\bar{\kappa}}{\bar{\kappa}_B} \leq \frac{27\pi\epsilon_0 mc f u_1^2}{16e^2 \nu_{m,2}} \quad (\text{A4})$$

$$\leq 0.936 \left(\frac{f}{0.1875}\right) \left(\frac{u_1}{10^3 \text{ km s}^{-1}}\right)^2 \left(\frac{\nu_{m,2}}{10^{17} \text{ Hz}}\right)^{-1}, \quad (\text{A5})$$

where

$$\bar{\kappa} = \left(\frac{B_1^2}{u_1} \kappa_1 + \frac{B_2^2}{u_2} \kappa_2\right) \left(\frac{B_1^2}{u_1} + \frac{B_2^2}{u_2}\right)^{-1}, \quad (\text{A6})$$

$$\bar{\kappa}_B = \left(\frac{B_1^2}{u_1} \kappa_{B,1} + \frac{B_2^2}{u_2} \kappa_{B,2}\right) \left(\frac{B_1^2}{u_1} + \frac{B_2^2}{u_2}\right)^{-1}, \quad (\text{A7})$$

the upstream and downstream Bohm diffusion coefficients $\kappa_{B,1}$ and $\kappa_{B,2}$ are equal to $p_m c/(3eB_1)$ and $p_m c/(3eB_2)$, respectively, at a momentum $p = p_m$, $\nu_{m,2}$ is the critical frequency of an electron with this momentum in a magnetic field $B = B_2$,

$$f = \frac{r - 1}{r[r + (B_1/B_2)]}, \quad (\text{A8})$$

and the compression ratio $r = u_1/u_2$. The value of 0.1875 in equation (A5) was calculated assuming $r = 4$ and $B_1/B_2 \approx 0$. If the compression ratio is greater than 4 or B_1/B_2 is significantly larger than zero, then $f < 0.1875$. In no case can f be larger than 0.25. If $B_1 = B_2$, then equation (A5) is identical to the analogous equation in Stage et al. (2006). Equation (A5) is similar to equation (22) of Aharonian & Atoyan (1999), equation (12) of Lazendic et al. (2004), equation (A.4) of Yamazaki et al. (2004), and equation (22) of Parizot et al. (2006), except these authors use the peak frequency instead of the critical frequency. The latter three also use $\sin \theta = 1$ instead of $\pi/4$.

REFERENCES

- Aharonian, F. A., et al. 2005, *A&A*, 437, 135
- Aharonian, F. A., & Atoyan, A. M. 1999, *A&A*, 351, 330
- Allen, G. E., Petre, R., & Gotthelf, E. V. 2001, *ApJ*, 558, 739
- Anders, E., & Grevesse, N. 1989, *Geochim. Cosmochim. Acta*, 53, 197
- Anderson, M. C., & Rudnick, L. 1996, *ApJ*, 456, 234
- Bamba, A., Yamazaki, R., Ueno, M., & Koyama, K. 2003, *ApJ*, 589, 827
- Bamba, A., et al. 2008, *PASJ*, 60, S153
- Bell, A. R. 1987, *MNRAS*, 225, 615
- . 2004, *MNRAS*, 353, 550
- Bell, A. R., & Lucek, S. G. 2001, *MNRAS*, 321, 433
- Berezhko, E. G., & Ellison, D. C. 1999, *ApJ*, 526, 385
- Berezhko, E. G., Ksenofontov, L. T., & Völk, H. J. 2002 *A&A*, 395, 943
- Blondin, J. M., & Ellison, D. C. 2001, *ApJ*, 560, 244
- Blumenthal, G. R., & Gould, R. J. 1970, *Rev. Mod. Phys.*, 42, 237
- Cassam-Chenai, G., Hughes, J. P., Reynoso, E. M., Badenes, C., & Moffett, D. 2008, *ApJ*, 680, 1180
- Chevalier, R. A. 1983, *ApJ*, 272, 765

- Decourchelle, A., Ellison, D. C., & Ballet, J. 2000, *ApJ*, 543, L57
- DeLaney, T., Koralesky, B., Rudnick, L., & Dickel, J. R. 2002, *ApJ*, 580, 914
- Drury, L. O’C., Markiewicz, W. J., & Völk, H. J. 1989, *A&A*, 225, 179
- Dwarkadas, V. V., & Chevalier, R. A. 1998, *ApJ*, 497, 807
- Dyer, K. K., Reynolds, S. P., Borkowski, K. J., Allen, G. E., & Petre, R. 2001, *ApJ*, 551, 439
- Ellison, D. C., Berezhko, E. G., & Baring, M. G. 2000, *ApJ*, 540, 292
- Ellison, D. C., & Reynolds, S. P. 1991, *ApJ*, 382, 242
- Ellison, D. C., Slane, P., & Gaensler, B. M. 2001, *ApJ*, 563, 191
- Eriksen, K. A., Morse, J. A., Kirshner, R. P., & Winkler, P. F. 2001, in *AIP Conf. Proc.* 565, Young Supernova Remnants, ed. S. S. Holt & U. Hwang (Melville, NY: AIP), 193
- Finkelstein, S. L., et al. 2006, *ApJ*, 641, 919
- Flanagan, K. A., Canizares, C. R., Dewey, D., Houck, J. C., Fredericks, A. C., Schattenburg, M. L., Markert, T. H., & Davis, D. S. 2004, *ApJ*, 605, 230
- Gardner, F. F., & Milne, D. K. 1965, *AJ*, 70, 754
- Ghavamian, P., Winkler, P. F., Raymond, J. C., & Long, K. S. 2002, *ApJ*, 572, 888
- Green D. A. 2006, *A Catalogue of Galactic Supernova Remnants* (ver. 2006 April; Cambridge: Cavendish Lab.), <http://www.mrao.cam.ac.uk/surveys/snrs>
- Houck, J. C., & Allen, G. E. 2006, *ApJS*, 167, 26
- Houck, J. C., & DeNicola, L. A. 2000, in *ASP Conf. Ser.* 216, *Astronomical Data Analysis Software and Systems IX*, ed. N. Manset, C. Veillet, & D. Crabtree (San Francisco: ASP), 591
- Hughes, J. P., Rakowski, C. E., & Decourchelle, A. 2000, *ApJ*, 543, L61
- Jokipii, J. R. 1987, *ApJ*, 313, 842
- Jones, T. J., Rudnick, L., DeLaney, T., & Bowden, J. 2003, *ApJ*, 587, 227
- Ksenofontov, L. T., Berezhko, E. G., & Völk, H. J. 2005, *A&A*, 443, 973

- Koyama, K., Petre, R., Gotthelf, E. V., Hwang, U., Matsuura, M., Ozaki, M., & Holt, S. S. 1995, *Nature*, 378, 255
- Kundu, M. R. 1970, *ApJ*, 162, 17
- Lagage, P.-O., & Cesarsky, C. J. 1983, *A&A*, 125, 249
- Laming, J. M., Raymond, J. C., McLaughlin, B. M., & Blair, W. P. 1996, *ApJ*, 472, 267
- Lazendic, J. S., Slane, P. O., Gaensler, B. M., Reynolds, S. P., Plucinsky, P. P., & Hughes, J. P. 2004, *ApJ*, 602, 271
- Long, K. S., Reynolds, S. P., Raymond, J. C., Winkler, P. F., Dyer, K. K., Petre, R. 2003, *ApJ*, 586, 1162
- Lucek, S. G. & Bell, A. R. 2000, *MNRAS*, 314, 65
- Milne, D. K. 1971, *Australian. J. Phys.*, 24, 757
- Milne, D. K., & Dickel, J. R. 1975, *Australian. J. Phys.*, 28, 209
- Moffett, D. A., Goss, W. M., & Reynolds, S. P. 1993, *AJ*, 106, 1566
- Parizot, E., Marcowith, A., Ballet, J., & Gallant, Y. A. 2006, *A&A*, 453, 387
- Pohl, M., Yan, H., & Lazarian, A. 2005, *ApJ*, 626, L101
- Protheroe, R. J. 2004, *Astropart. Phys.*, 21, 415
- Reynolds, S. P., & Ellison, D. C. 1992, *ApJ*, 399, L75
- Reynolds, S. P., & Gilmore, D. M. 1986, *AJ*, 92, 1138
- Roger, R. S., Milne, D. K., Kesteven, M. J., Wellington, K. J., & Haynes, R. F. 1988, *ApJ*, 332, 940
- Rothenflug, R., Ballet, J., Dubner, G., Giacani, E., Decourchelle, A., & Ferrando, P. 2004, *A&A*, 425, 121
- Schaefer, B. E. 1996, *ApJ*, 459, 438
- Stage, M. D., Allen, G. E., Houck, J. C., & Davis, J. E. 2006, *Nature Phys.*, 2, 614
- Stephenson, F. R., Clark, D. H., & Crawford, D. F. 1977, *MNRAS*, 180, 567
- Tanimori, T., et al. 1998, *ApJ*, 497, L25

- Uchiyama, Y., Aharonian, F. A., & Takahashi, T. 2003, *A&A*, 400, 567
- Vink, J., Bleeker, J., van der Heyden, K., Bykov, A., Bamba, A., & Yamazaki, R. 2006, *ApJ*, 648, L33
- Völk, H. J., Berezhko, E. G., & Ksenofontov, L. T. 2005, *A&A*, 433, 229
- Völk, H. J., & Biermann, P. L. 1988, *ApJ*, 333, L65
- Warren, J. S., et al. 2005, *ApJ*, 634, 376
- Webb, G. M., Drury, L. O’C., & Biermann, P. 1984, *A&A*, 137, 185
- Winkler, P. F., Gupta, G., & Long, K. S. 2003, *ApJ*, 585, 324
- Winkler, P. F., & Long, K. S. 1997, *ApJ*, 491, 829
- Yamazaki, R., Yoshida, T., Terasawa, T., Bamba, A., & Koyama, K. 2004, *A&A*, 416, 595
- Zirakashvili, V. N., & Aharonian, F. 2007, *A&A*, 465, 695

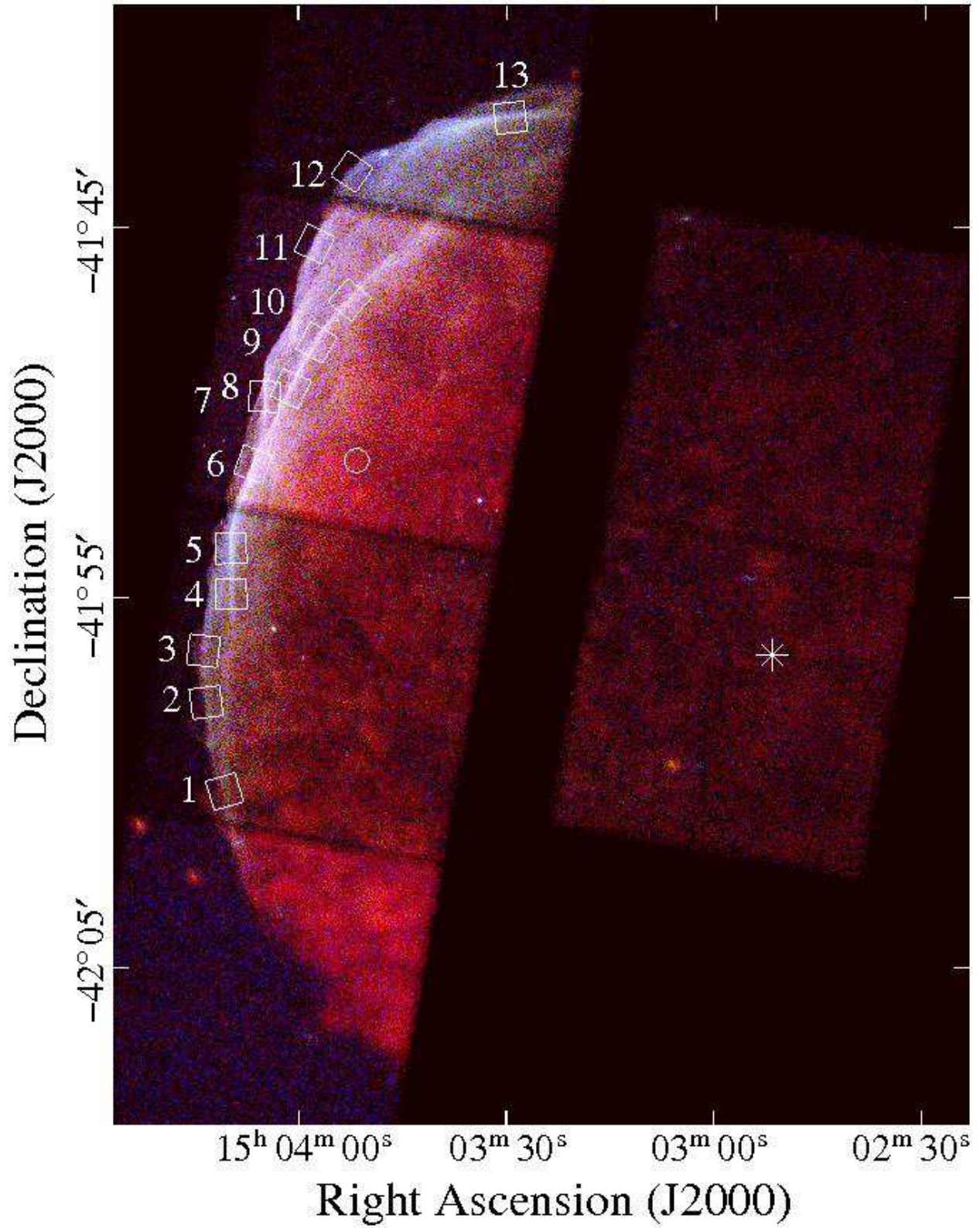


Fig. 1.— Color-coded ACIS image of the northeastern rim of SN 1006. Red, green, and blue correspond to the energy bands 0.4–1, 1–2, and 2–7 keV, respectively. Most of the emission at energies greater than 1 keV is concentrated in the whitish filaments along the rim. The edges of the six square CCDs used to observe the remnant are evident. The relatively high brightnesses of the CCD with the circle on it and the CCD in the lower left corner are due to enhanced low-energy sensitivities for these two devices. The circle at $\alpha = 15^{\text{h}}03^{\text{m}}51.56^{\text{s}}$ and $\delta = -41^{\circ}51'18.8''$ (J2000) indicates the location of the nominal aim point of the telescope. The asterisk at $\alpha = 15^{\text{h}}02^{\text{m}}51.7^{\text{s}}$ and $\delta = -41^{\circ}56'33.0''$ is the location of the center of the supernova remnant (Winkler & Long 1997). The 13 squares are the X-ray spectral extraction regions.

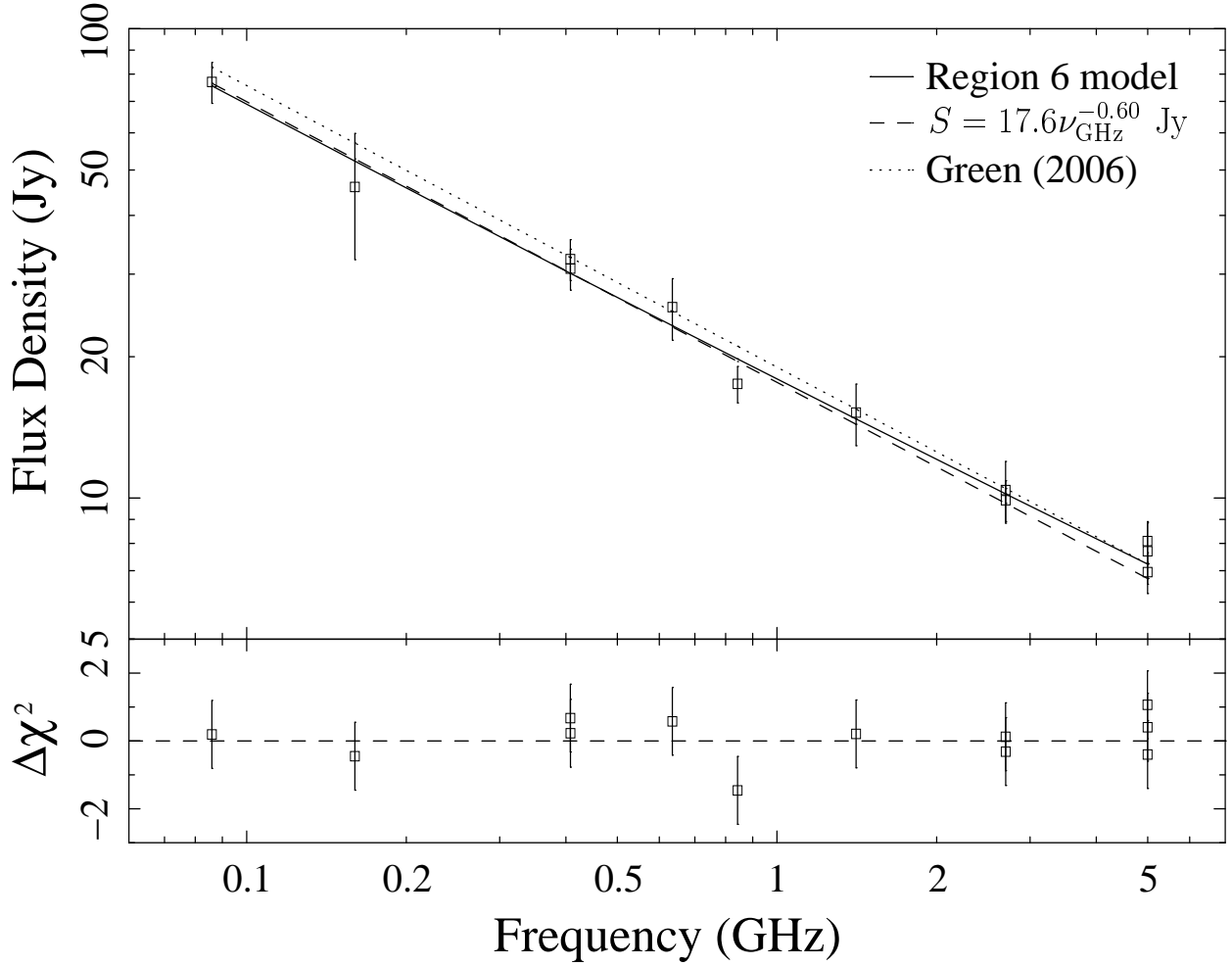


Fig. 2.— Radio spectrum for the entire supernova remnant SN 1006. *Top:* The data points (Table 1) and three models. The dashed line is the best-fit power law, $S(\nu) = 17.6_{-4.8}^{+6.3}[\nu/(1 \text{ GHz})]^{-\alpha}$ Jy, where $\alpha = 0.60_{-0.09}^{+0.08}$. The dotted line is a power law using Green’s (2006) spectral parameters [$S(\nu) = 19[\nu/(1 \text{ GHz})]^{-0.6}$ Jy]. The solid line is the best-fit (curved) synchrotron model for region 6 divided by the factor 0.00175 (see Table 2). *Bottom:* Differences between the data points and the solid line, divided by the uncertainties in the data points.

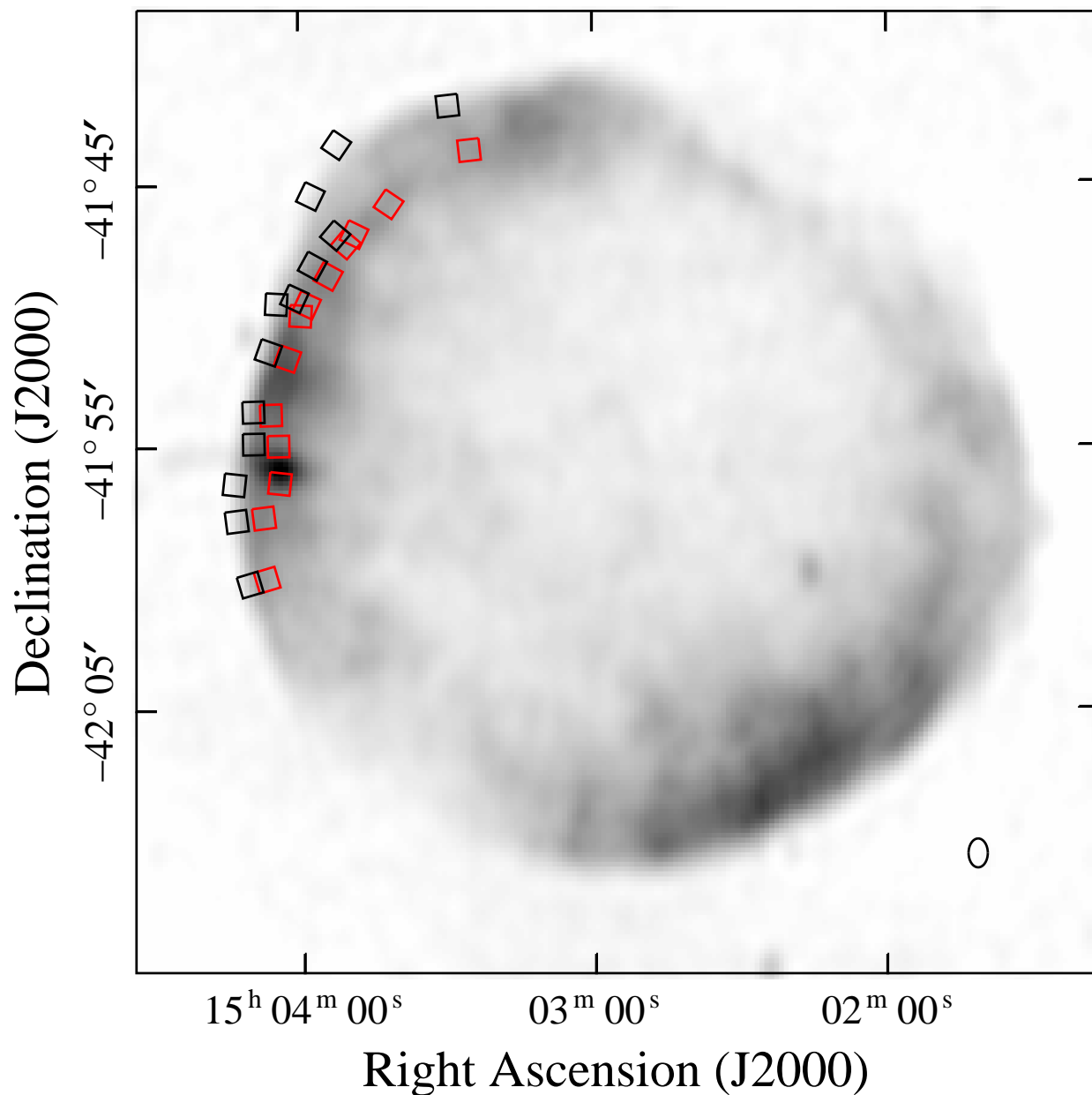


Fig. 3.— An 843 MHz MOST image of SN 1006, courtesy of R. Roger (Roger et al. 1988). The ellipse at lower right indicates the half-power beamwidth. The 13 black squares are the locations of the X-ray spectral extraction regions. These regions were used to obtain the “cospatial” radio fluxes (Tables 2 and 3). The red squares are the locations used to obtain the peak radio fluxes (Tables 4 and 5). The ratios of the flux densities of the black and red regions to the total flux density are listed in the ζ columns of Tables 2–5. The bright spot at about $\alpha = 15^{\text{h}}04^{\text{m}}04^{\text{s}}$ and $\delta = -41^{\circ}55'48''$ is produced by an extragalactic source (Reynolds & Gilmore 1986).

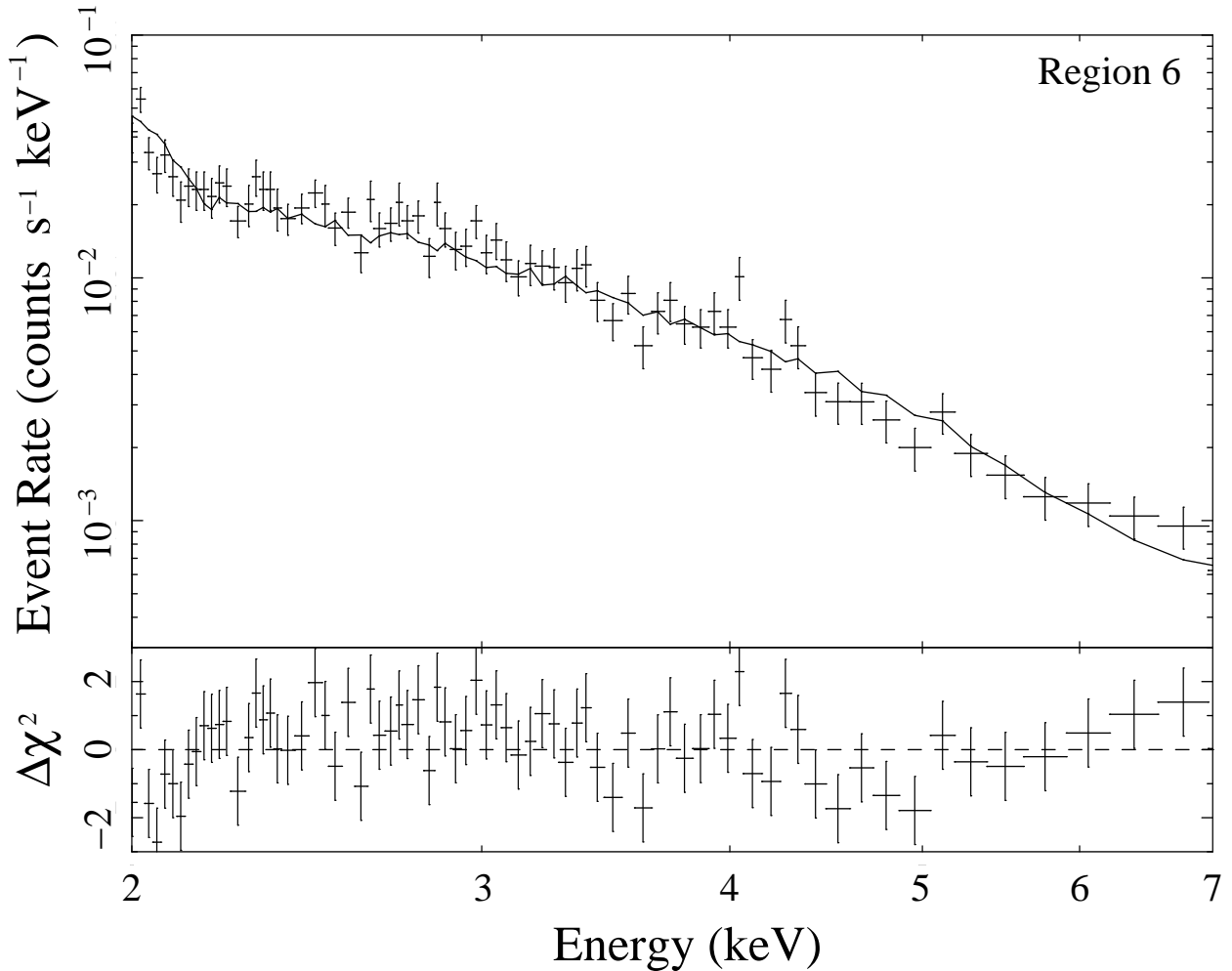


Fig. 4.— ACIS spectrum for region 6 (see Fig. 1) of the bright northeastern rim of SN 1006. *Top*: Sum of the source and background spectra (*data points*) and the sum of the best-fit model and background spectra (*solid line*). The model displayed here includes spectral curvature as a free parameter (see Table 2). *Bottom*: Differences between the data points and the solid line, divided by the uncertainties in the data points.

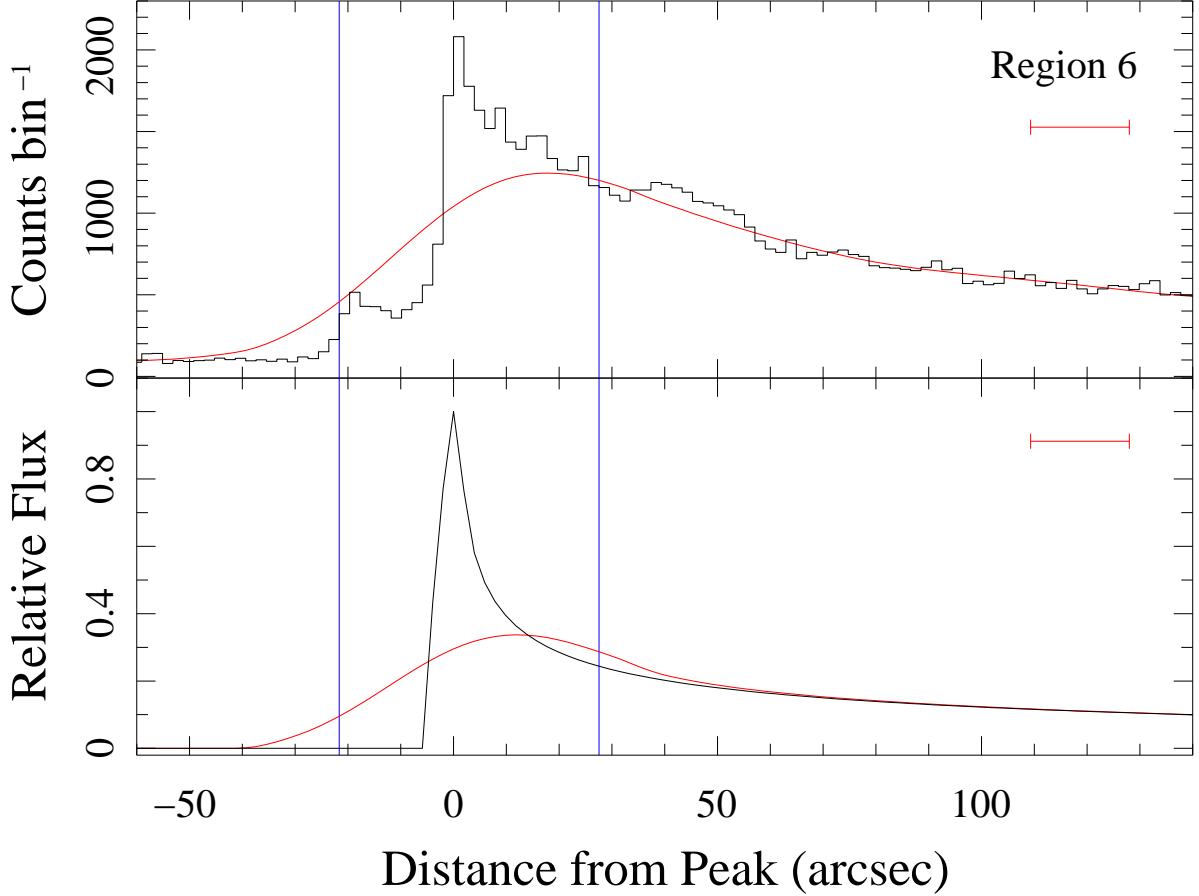


Fig. 5.— X-ray emission profiles along a $49''$ -wide strip passing through region 6 toward the center of SN 1006. The black histogram in the top panel is the 2–7 keV ACIS data. For comparison, the black line in the bottom panel is a model based on the assumption that the emission is produced in a uniformly emitting shell that is $6''$ wide. The red curves are the data and model smoothed to the resolution of the MOST image. (The horizontal red bars are the 1σ widths of the Gaussian smoothing function.) The reduction in spatial resolution causes the peak to shift downstream, but the offset is small compared with the width of the extraction region. (The blue lines are the boundaries of region 6.) Therefore, it seems unlikely that the offsets between the X-ray and radio peaks (see Fig. 3 and Tables 4 and 5) are due to the different X-ray and radio resolutions.

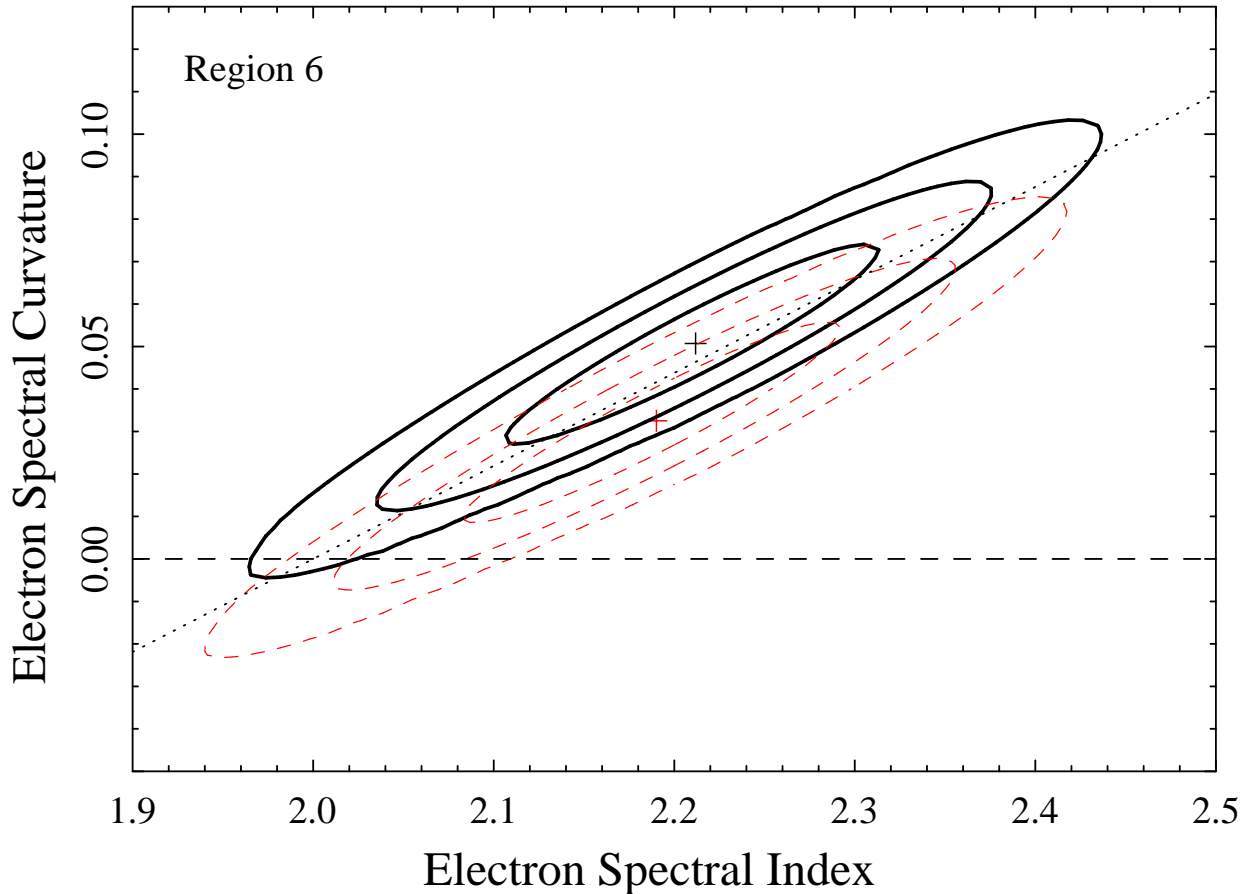


Fig. 6.— The 1, 2, and 3 σ confidence contours for region 6 (see Fig. 1) in the parameter space defined by the electron spectral index Γ and electron spectral curvature a (see eq. [2]). The solid black and dashed red contours are the results obtained using the cospatial (Table 2) and peak (Table 4) radio fluxes, respectively. The plus signs indicate the best-fit values of the index and curvature. The dotted black line is the expected relationship between Γ and a (eq. [7]). The dashed black line is the line along which the electron spectrum is not curved (i.e., $a = 0$). For region 6, a positive curvature (i.e., a result above the dashed line) is favored at about the 2.7 and 1.6 σ confidence levels for the black and red contours, respectively.

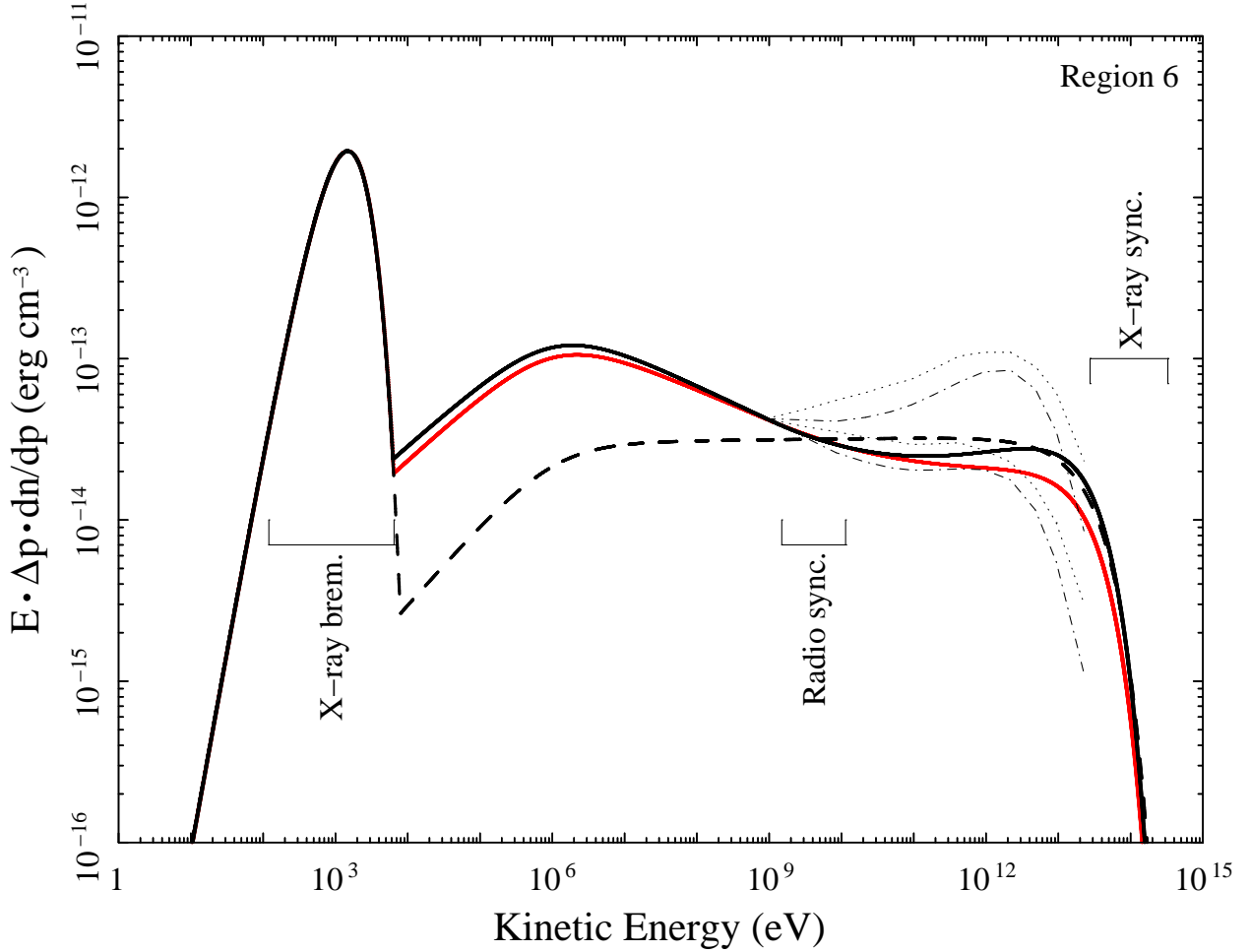


Fig. 7.— Best-fit electron number density spectra for region 6 (see Fig. 1). The solid and dashed black lines are the curved (Table 2) and uncurved (Table 3) models, respectively, using the cospatial radio flux. The solid red line is the curved model using the peak radio flux (Table 4). The upper dotted and dot-dashed curves are the models for the proton (not electron) spectrum of SN 1006 presented by Ellison et al. (2000). These lines are plotted only for momenta $p > mc$ (i.e., the range of momenta to which our fits are sensitive) and are normalized to the solid black line at a kinetic energy of 0.9 GeV. As described in the text, the lower dotted and dot-dashed curves are the same pair of models multiplied by $[E/(0.9 \text{ GeV})]^{-0.2}$. The amounts of spectral curvature in the solid lines are consistent with the amounts of curvature in the lower dotted and dot-dashed curves. From left to right, the three bracketed energy bands contain the electrons that are primarily responsible for the observed thermal bremsstrahlung, radio synchrotron, and X-ray synchrotron emission.

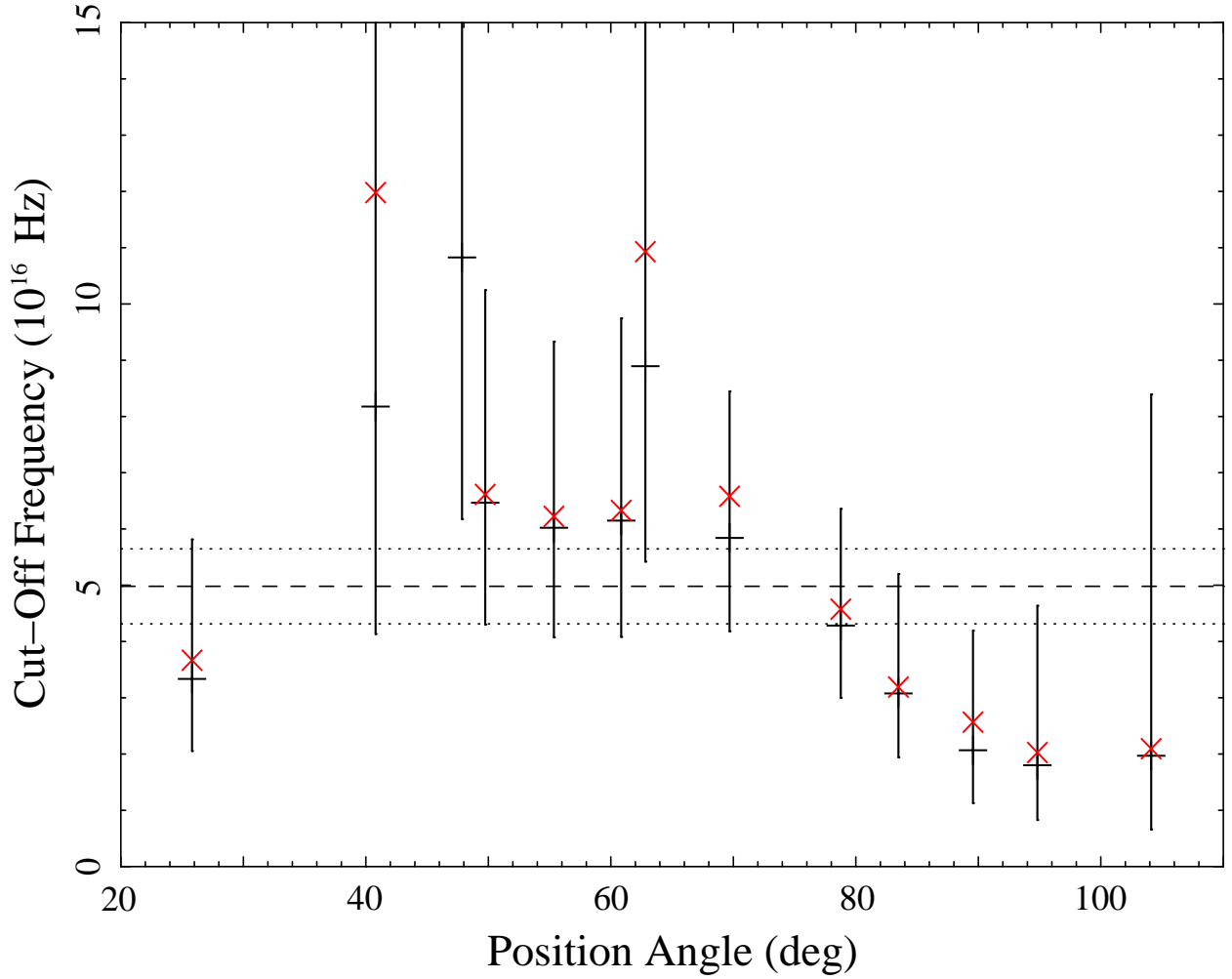


Fig. 8.— Cutoff frequency as a function of position angle (measured counterclockwise from north through east). From right to left, the 13 pairs of points are for regions 1–13, respectively (see Fig. 1). The black data points and 90% confidence intervals are the results obtained using a curved electron spectrum and the cospatial radio fluxes (Table 2). The red data points, which have similar confidence intervals, are the results obtained using the peak radio fluxes (Table 4). The dashed line is the weighted mean value (4.98×10^{16} Hz) of the black points. The corresponding 90% confidence level interval [$(4.31\text{--}5.65) \times 10^{16}$ Hz] lies between the two dotted lines. A constant value for the cutoff frequency can be excluded at the 2.5σ confidence level.

Table 1. Radio Data

ν (GHz)	S (Jy)	ΔS (Jy)	Refs.
0.086	77	7.7 ^a	1
0.16	46	13.8	1
0.408	32.3	3.2	1
0.408	30.8	3.1 ^a	2
0.635	25.5	3.8	1
0.843	17.5	1.5	3
1.41	15.2	2.3	1
2.7	10.4	1.6	1
2.7	9.9	1.0 ^a	1, 4
5.0	7.7	1.2	1
5.0	7.0	0.7 ^a	5
5.0	8.1	0.8 ^a	6

Note.—The table lists the frequencies ν , flux densities S , and 1σ flux density uncertainties ΔS used for the spectral analysis. The quantities S and ΔS are for the emission from the entire supernova remnant.

^aSince no uncertainty was reported, it is assumed to be 10% of S . The results of our spectral fits are insensitive to the assumed fractional uncertainty at least for fractions between 5% and 20%.

References.—(1) Milne

1971; (2) Stephenson et al.
1977; (3) Roger et al. 1988;
(4) Gardner & Milne 1965;
(5) Kundu 1970; (6) Milne &
Dickel 1975.

Table 2. Best-Fit Parameters Using the Curved Model and ‘‘Cospatial’’ Radio Fluxes

Region	α_X (J2000)	δ_X (J2000)	ϕ (deg)	ζ ($\times 10^{-4}$)	Γ^a	a	ν_m (10^{16} Hz)	χ^2/dof	$P_{\Delta\chi^2}^b$
1	15 04 10.7	−42 00 15	104.1	10	$2.24^{+0.16}_{-0.16}$	$0.050^{+0.070}_{-0.059}$	$2.0^{+6.4}_{-1.3}$	8.4/18	0.17
2	15 04 13.3	−41 57 51	94.8	8.9	$2.27^{+0.13}_{-0.15}$	$0.071^{+0.051}_{-0.047}$	$1.8^{+2.8}_{-1.0}$	12.9/22	0.012
3	15 04 13.7	−41 56 27	89.6	6.9	$2.27^{+0.13}_{-0.13}$	$0.080^{+0.039}_{-0.039}$	$2.1^{+2.1}_{-1.0}$	11.0/27	0.00055
4	15 04 09.7	−41 54 54	83.5	24	$2.22^{+0.12}_{-0.12}$	$0.051^{+0.030}_{-0.031}$	$3.1^{+2.1}_{-1.2}$	50.2/46	0.0073
5	15 04 09.7	−41 53 41	78.8	15	$2.23^{+0.11}_{-0.12}$	$0.060^{+0.026}_{-0.027}$	$4.3^{+2.1}_{-1.3}$	71.4/63	0.00033
6	15 04 06.5	−41 51 25	69.7	18	$2.21^{+0.11}_{-0.11}$	$0.051^{+0.025}_{-0.026}$	$5.8^{+2.6}_{-1.6}$	91.5/84	0.0014
7	15 04 04.8	−41 49 35	62.8	11	$2.19^{+0.11}_{-0.11}$	$0.036^{+0.027}_{-0.027}$	$8.9^{+6.9}_{-3.5}$	69.2/60	0.030
8	15 04 01.1	−41 49 22	60.8	17	$2.20^{+0.11}_{-0.11}$	$0.042^{+0.026}_{-0.027}$	$6.1^{+3.6}_{-2.0}$	69.4/71	0.011
9	15 03 57.3	−41 48 08	55.4	19	$2.20^{+0.11}_{-0.11}$	$0.042^{+0.026}_{-0.027}$	$6.0^{+3.3}_{-1.9}$	73.0/72	0.010
10	15 03 52.6	−41 46 58	49.7	17	$2.20^{+0.11}_{-0.12}$	$0.042^{+0.026}_{-0.027}$	$6.5^{+3.7}_{-2.2}$	71.4/69	0.011
11	15 03 57.7	−41 45 28	47.9	3.8	$2.20^{+0.11}_{-0.11}$	$0.057^{+0.028}_{-0.028}$	$10.8^{+10.3}_{-4.6}$	65.3/61	0.00079
12	15 03 52.3	−41 43 31	40.8	3.0	$2.21^{+0.11}_{-0.11}$	$0.060^{+0.032}_{-0.032}$	$8.2^{+10.9}_{-4.1}$	32.2/37	0.0018
13	15 03 29.5	−41 42 03	25.8	9.5	$2.25^{+0.11}_{-0.12}$	$0.070^{+0.031}_{-0.031}$	$3.3^{+2.5}_{-1.2}$	35.5/42	0.00023
Mean					$2.221^{+0.013}_{-0.012}$	0.054 ± 0.006			

Notes.—For each region, the table includes a list of the right ascension (α_X), declination (δ_X), and position-angle (ϕ) coordinates of the center of the X-ray region, the 843 MHz flux divided by the total 843 MHz flux (ζ), the best-fit differential electron spectral index Γ , curvature parameter a , and cutoff frequency ν_m , the value of χ^2 per degree of freedom (χ^2/dof), and the probability ($P_{\Delta\chi^2}$) that the difference between the value of χ^2 in Table 3 and the value in this table is due to chance. The uncertainties, which include only the statistical contributions, are reported at the 90% confidence level. These uncertainties were used to compute the weighted

mean values of Γ and a . Units of right ascension are hours, minutes, and seconds, and units of declination are degrees, arcminutes, and arcseconds.

^aAs described in the text, the spectral indices are not independent from region to region.

^bIncluding curvature as a free parameter significantly improves the quality of the fit for most regions.

Table 3. Best-Fit Parameters Using the Uncurved Model and “Cospatial” Radio Fluxes

Region	α_X (J2000)	δ_X (J2000)	ϕ (deg)	ζ ($\times 10^{-4}$)	Γ	a^a	ν_m (10^{16} Hz)	χ^2/dof
1	15 04 10.7	−42 00 15	104.1	10	$2.12^{+0.08}_{-0.08}$	0	$5.8^{+5.3}_{-2.4}$	10.3/19
2	15 04 13.3	−41 57 51	94.8	8.9	$2.08^{+0.07}_{-0.08}$	0	$6.8^{+6.0}_{-2.8}$	19.2/23
3	15 04 13.7	−41 56 27	89.6	6.9	$2.03^{+0.07}_{-0.07}$	0	$7.7^{+6.1}_{-3.0}$	22.9/28
4	15 04 09.7	−41 54 54	83.5	24	$2.04^{+0.05}_{-0.06}$	0	$5.8^{+3.1}_{-1.8}$	57.4/47
5	15 04 09.7	−41 53 41	78.8	15	$1.98^{+0.04}_{-0.05}$	0	$7.6^{+3.3}_{-2.1}$	84.3/64
6	15 04 06.5	−41 51 25	69.7	18	$1.99^{+0.04}_{-0.03}$	0	$9.2^{+3.6}_{-2.4}$	101.7/85
7	15 04 04.8	−41 49 35	62.8	11	$2.05^{+0.05}_{-0.04}$	0	$14.7^{+9.3}_{-5.2}$	73.9/61
8	15 04 01.1	−41 49 22	60.8	17	$2.03^{+0.04}_{-0.04}$	0	$9.8^{+4.7}_{-3.0}$	75.9/72
9	15 03 57.3	−41 48 08	55.4	19	$2.03^{+0.04}_{-0.04}$	0	$9.4^{+4.3}_{-2.7}$	79.6/73
10	15 03 52.6	−41 46 58	49.7	17	$2.03^{+0.04}_{-0.04}$	0	$10.3^{+5.0}_{-3.1}$	77.9/70
11	15 03 57.7	−41 45 28	47.9	3.8	$2.00^{+0.04}_{-0.05}$	0	$28.4^{+26.8}_{-12.1}$	76.5/62
12	15 03 52.3	−41 43 31	40.8	3.0	$2.02^{+0.06}_{-0.06}$	0	$29.6^{+39.0}_{-14.4}$	41.9/38
13	15 03 29.5	−41 42 03	25.8	9.5	$2.00^{+0.05}_{-0.06}$	0	$8.8^{+5.6}_{-3.1}$	49.1/43
Mean					$2.031^{+0.017}_{-0.016}$	0		

Notes.—See the caption for Table 2. Units of right ascension are hours, minutes, and seconds, and units of declination are degrees, arcminutes, and arcseconds.

^aThe curvature parameter was fixed at zero.

Table 4. Best-Fit Parameters Using the Curved Model and Peak Radio Fluxes

Region	α_R (J2000)	δ_R (J2000)	$\Delta\Psi$ (arcmin)	ζ ($\times 10^{-4}$)	Γ^a	a	ν_m (10^{16} Hz)	χ^2/dof	$P_{\Delta\chi^2}^b$
1	15 04 07.1	-42 00 05	0.68	17	$2.21^{+0.16}_{-0.16}$	$0.035^{+0.069}_{-0.060}$	$2.1^{+7.3}_{-1.4}$	8.5/18	0.35
2	15 04 07.7	-41 57 44	1.04	22	$2.22^{+0.14}_{-0.15}$	$0.042^{+0.050}_{-0.047}$	$2.0^{+3.5}_{-1.1}$	13.1/22	0.15
3	15 04 04.4	-41 56 25	1.73	30	$2.20^{+0.12}_{-0.14}$	$0.031^{+0.040}_{-0.038}$	$2.6^{+3.0}_{-1.3}$	11.3/27	0.18
4	15 04 04.6	-41 55 00	0.95	30	$2.21^{+0.12}_{-0.12}$	$0.043^{+0.031}_{-0.030}$	$3.2^{+2.2}_{-1.2}$	50.2/46	0.021
5	15 04 06.1	-41 53 48	0.67	22	$2.21^{+0.11}_{-0.12}$	$0.048^{+0.026}_{-0.027}$	$4.6^{+2.3}_{-1.4}$	71.5/63	0.0037
6	15 04 02.6	-41 51 40	0.77	31	$2.19^{+0.11}_{-0.12}$	$0.033^{+0.025}_{-0.026}$	$6.6^{+3.1}_{-2.0}$	91.8/84	0.040
7	15 03 59.9	-41 50 02	1.03	26	$2.16^{+0.11}_{-0.11}$	$0.010^{+0.027}_{-0.028}$	$10.9^{+9.6}_{-4.5}$	69.6/60	0.55
8	15 03 58.6	-41 49 37	0.53	20	$2.20^{+0.11}_{-0.12}$	$0.037^{+0.027}_{-0.026}$	$6.3^{+3.8}_{-2.1}$	69.5/71	0.023
9	15 03 54.1	-41 48 31	0.72	22	$2.20^{+0.11}_{-0.12}$	$0.037^{+0.026}_{-0.027}$	$6.2^{+3.5}_{-2.0}$	73.0/72	0.023
10	15 03 50.5	-41 47 18	0.52	19	$2.20^{+0.11}_{-0.12}$	$0.038^{+0.027}_{-0.026}$	$6.6^{+3.9}_{-2.2}$	71.4/69	0.019
11	15 03 47.8	-41 46 56	2.35	16	$2.16^{+0.11}_{-0.11}$	$0.013^{+0.027}_{-0.028}$	$16.0^{+19.2}_{-7.6}$	65.7/61	0.46
12	15 03 41.7	-41 45 48	3.02	15	$2.16^{+0.11}_{-0.11}$	$0.010^{+0.032}_{-0.031}$	$12.0^{+20.7}_{-6.4}$	32.6/37	0.59
13	15 03 25.2	-41 43 45	1.88	17	$2.22^{+0.12}_{-0.12}$	$0.052^{+0.031}_{-0.031}$	$3.7^{+2.8}_{-1.5}$	35.6/42	0.0062
Mean					2.198 ± 0.011	$0.033^{+0.007}_{-0.008}$			

Notes.—For each region, the table includes a list of the right ascension (α_R) and declination (δ_R) coordinates of the center of the radio region, the angular distance between the centers of the X-ray (see Table 2) and radio regions $\Delta\Psi$, the 843 MHz flux divided by the total 843 MHz flux (ζ), the best-fit differential electron spectral index Γ , curvature parameter a , and cutoff frequency ν_m , the value of χ^2 per degree of freedom (χ^2/dof), and the probability ($P_{\Delta\chi^2}$) that the difference between the value of χ^2 in Table 5 and the value in this table is due to chance. The uncertainties, which include only the statistical contributions, are reported at the 90% confidence

level. These uncertainties were used to compute the weighted mean values of Γ and a . Units of right ascension are hours, minutes, and seconds, and units of declination are degrees, arcminutes, and arcseconds.

^aAs described in the text, the spectral indices are not independent from region to region.

^bIncluding curvature as a free parameter improves the quality of the fit for every region.

Table 5. Best-Fit Parameters Using the Uncurved Model and Peak Radio Fluxes

Region	α_R (J2000)	δ_R (J2000)	$\Delta\Psi$ (arcmin)	ζ ($\times 10^{-4}$)	Γ	a^a	ν_m (10^{16} Hz)	χ^2/dof
1	15 04 07.1	–42 00 05	0.68	17	$2.13^{+0.08}_{-0.08}$	0	$4.3^{+3.5}_{-1.7}$	9.4/19
2	15 04 07.7	–41 57 44	1.04	22	$2.11^{+0.07}_{-0.08}$	0	$4.3^{+3.1}_{-1.6}$	15.2/23
3	15 04 04.4	–41 56 25	1.73	30	$2.10^{+0.07}_{-0.06}$	0	$4.3^{+2.6}_{-1.5}$	13.1/28
4	15 04 04.6	–41 55 00	0.95	30	$2.05^{+0.06}_{-0.05}$	0	$5.5^{+2.9}_{-1.7}$	55.6/47
5	15 04 06.1	–41 53 48	0.67	22	$2.01^{+0.05}_{-0.04}$	0	$7.3^{+3.1}_{-2.0}$	79.9/64
6	15 04 02.6	–41 51 40	0.77	31	$2.05^{+0.04}_{-0.04}$	0	$8.9^{+3.4}_{-2.3}$	96.1/85
7	15 03 59.9	–41 50 02	1.03	26	$2.12^{+0.05}_{-0.04}$	0	$12.6^{+7.7}_{-4.3}$	70.0/61
8	15 03 58.6	–41 49 37	0.53	20	$2.04^{+0.05}_{-0.04}$	0	$9.6^{+4.7}_{-2.9}$	74.6/72
9	15 03 54.1	–41 48 31	0.72	22	$2.04^{+0.04}_{-0.04}$	0	$9.2^{+4.2}_{-2.6}$	78.2/73
10	15 03 50.5	–41 47 18	0.52	19	$2.04^{+0.04}_{-0.04}$	0	$10.1^{+5.0}_{-3.0}$	76.9/70
11	15 03 47.8	–41 46 56	2.35	16	$2.12^{+0.04}_{-0.05}$	0	$20.0^{+16.4}_{-8.0}$	66.2/62
12	15 03 41.7	–41 45 48	3.02	15	$2.13^{+0.06}_{-0.06}$	0	$15.0^{+14.1}_{-6.4}$	32.9/38
13	15 03 25.2	–41 43 45	1.88	17	$2.04^{+0.05}_{-0.06}$	0	$7.5^{+4.6}_{-2.5}$	43.1/43
Mean					$2.073^{+0.021}_{-0.020}$	0		

Note.—See the caption for Table 4. Units of right ascension are hours, minutes, and seconds, and units of declination are degrees, arcminutes, and arcseconds.

^aThe curvature parameter was fixed at zero.